THE JOURNAL OF PHYSICAL CHEMISTRY C
A JOURNAL OF THE AMERICAN CHEMICAL SOCIETY

pubs.acs.org/JPCC

Article

Deconstructing Interfacial Charge-Transfer and Exciton Dynamics in Functionalized Covalent Organic Frameworks: A Marcus−Hush and Diabatization Study

Sohini Khan and Anirban Mondal*

Cite This: https://doi.org/10.1021/acs.jpcc.6c03692

Read Online

ACCESS | Metrics & More | Article Recommendations | Supporting Information

ABSTRACT: Covalent organic frameworks (COFs) have emerged as promising photocatalysts for hydrogen evolution due to their tunable electronic structures and extended π-conjugation. However, a quantitative understanding of how excited-state dynamics and interfacial charge-transfer processes govern photocatalytic efficiency remains limited. In this work, we develop an integrated theoretical framework that links light absorption, exciton dynamics, and interfacial charge-transfer kinetics in substituted COFs, with direct relevance to experimentally measured hydrogen evolution rates. This framework explicitly treats photocatalysis as a sequence of coupled processes culminating in catalytically relevant charge-transfer events. Using a combination of real-time excited-state simulations and Projection Operator Diabatization (POD), we systematically investigate how chemical substitution modulates exciton delocalization, initial electronic coherence, and electronic couplings at the COF−sacrificial donor and COF−Pt cocatalyst interfaces. We show that halogen substitution induces distinct charge-carrier redistribution and separation behaviors, which translate into measurable differences in interfacial electronic couplings. By incorporating these couplings, energetic alignments, and reorganization energies into the Marcus−Hush formalism, we compute hole- and electron-transfer rates that reproduce the experimentally observed trends in hydrogen evolution efficiencies in a semiquantitative manner, without empirical fitting. Extending this analysis to hypothetical functionalizations (−Br, −CN, $-NO_2$, and −COOH) reveals that photocatalytic performance is governed by the emergence of energetically downhill, strongly coupled interfacial states rather than by static descriptors such as molecular dipole moment or binding energy alone. These findings establish charge-transfer rates as a mechanistically grounded descriptor of catalytic activity, demonstrating how subtle modifications in framework chemistry control excited-state dynamics and interfacial charge extraction in a unified manner. More broadly, the methodology established here provides a predictive, physical-chemistry-driven framework for the rational design and screening of efficient light-driven hydrogen evolution catalysts.

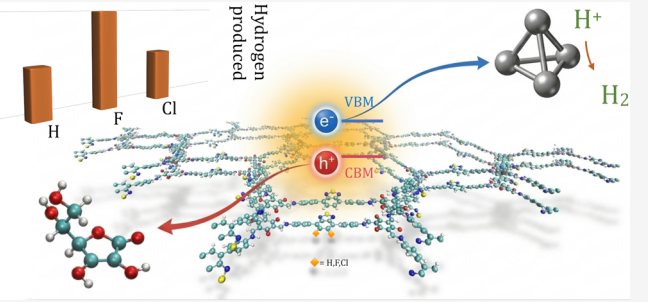

1. INTRODUCTION

Owing to the rapid depletion of fossil fuel reserves and the severe environmental consequences of their combustion, the transition to renewable and sustainable energy sources has become an urgent global priority.[1−3] Among the available alternatives, solar energy stands out as an abundant and inexhaustible resource capable of driving a wide range of chemical transformations when harnessed through suitable photocatalysts.[4,5] In this context, photocatalytic water splitting represents a particularly compelling strategy,[6] as it enables the generation of hydrogen fuel—an energy carrier with high gravimetric energy density and zero carbon emissions—directly from water using sunlight.[7−10] Achieving efficient hydrogen production via solar-driven water splitting would therefore address two critical challenges simultaneously: sustainable energy generation and environmental remediation. At its core, this process is governed by catalytic charge-transfer events occurring at photoactive interfaces, making a mechanistic understanding of these processes essential for advancing photocatalyst design.

Historically, photocatalytic water splitting has been dominated by inorganic semiconductor materials, largely due to their well-defined band gaps, favorable band-edge alignment with respect to proton reduction and water oxidation potentials, and high photostability under reaction conditions.[11−13] In addition to conventional semiconductors, other material classes such as plasmonic nanoparticles[14,15] and perovskites[16,17] have also demonstrated notable photocatalytic activity. However, these systems often suffer from limitations,

Received: June 5, 2026
Revised: August 13, 2026
Accepted: August 14, 2026

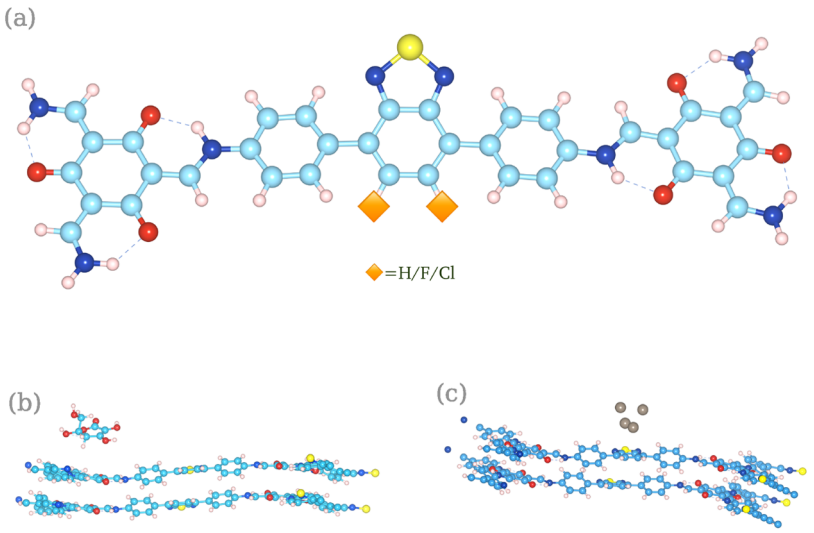

Figure 1. (a) Minimalist COF model employed for the excited-state calculations. The orange diamond indicates the substituted atom in the three COF variants (H, F, and Cl). (b) Structural model used for evaluating hole transfer rates, in which ascorbic acid is positioned on the TP ring along the *z*-axis. (c) Structural model used for evaluating electron transfer rates, featuring a tetrahedral Pt nanocluster placed on the benzothiadiazole ring along the *z*-axis. The atom color scheme is as follows: C (light blue), O (red), N (dark blue), H (light pink), S (yellow), and Pt (gray).

including high synthesis costs, poor long-term stability, or restricted structural tunability.[18−20] In contrast, covalent organic frameworks (COFs) have emerged as a promising class of organic photocatalysts, owing to their high surface areas, robust chemical and thermal stability, and modular, cost-effective synthetic routes.[21−23]

Photocatalytic COFs are particularly attractive because their optical and electronic properties can be tailored at the molecular level through judicious choice of building blocks. Many COFs are constructed from chromophoric units such as pyrene, triazine, or benzothiadiazole, which inherently absorb visible light and, when assembled into extended π-conjugated networks, enable absorption across a broad region of the solar spectrum.[24−26] Two-dimensional COFs, in particular, exhibit promising optoelectronic characteristics, including tunable band gaps, high photoluminescence quantum yields, and efficient in-plane charge transport, all of which are desirable for photocatalytic applications.[27−30] Importantly, these tunable properties directly influence key catalytic steps such as exciton dissociation, charge-carrier migration, and interfacial charge transfer, which ultimately determine hydrogen evolution efficiency.

Despite significant experimental progress, the molecular-level mechanisms governing photocatalytic hydrogen evolution in COFs remain incompletely understood. Most reported partial water-splitting reactions employing COFs rely on the presence of both a sacrificial electron donor and a cocatalyst, typically a noble metal such as Pt.[31] While the role of the cocatalyst in facilitating proton reduction is relatively well established, key mechanistic questions remain unresolved. In particular, the origin of the protons involved in hydrogen evolution (water versus sacrificial donor), the pathways of hole transfer among the COF, sacrificial agent, and water, and the factors controlling charge-carrier separation and migration are still subjects of debate.[32] This lack of molecular-level insight significantly hampers the rational design of next-generation COF photocatalysts with improved efficiency. Addressing these challenges requires a framework that explicitly connects excited-state processes to catalytically relevant charge-transfer events.

Previous computational studies on these COF systems have largely emphasized geometric descriptors such as torsional and dihedral angles, interlayer spacing, and planarity, and have attempted to rationalize photocatalytic trends primarily in terms of static charge separation between donor and acceptor fragments.[27,33,34] While these analyses capture certain qualitative correlations, static charge difference alone is insufficient to describe the complex, multistep processes governing photocatalytic hydrogen evolution. In particular, such approaches do not resolve the coupled dynamics of exciton formation, charge separation, carrier migration, and interfacial charge transfer, all of which are critical in determining the fate of photogenerated charge carriers and, ultimately, the catalytic efficiency.[35−37] A mechanistically consistent descriptor that links these processes to experimentally measurable catalytic activity remains largely lacking.

In this work, we address these limitations through a detailed theoretical investigation of three experimentally reported two-dimensional COFs constructed from a common structural motif comprising 1,3,5-triformylphloroglucinol (TP) nodes linked by benzothiadiazole units, forming extended π-conjugated frameworks. The structural models are adopted from ref 38. The COF with unsubstituted benzothiadiazole is denoted as H−COF, while its fluorine- and chlorine-substituted analogs are referred to as F-COF and Cl-COF, respectively. To further establish structure−activity relationships and assess the generality of substituent effects, we also examine a series of hypothetical COFs incorporating Br-, CN-, NO_2-, and COOH- functionalities, denoted as Br-COF, CN-COF, NO_2−COF, and COOH−COF. Building on this material platform, we move beyond static structural descriptors and develop a comprehensive structure−property framework based on density functional theory (DFT) and excited-state simulations that explicitly capture the photophysics of COF fragments under electromagnetic perturbation. Crucially, this framework is designed to elucidate catalytically relevant charge-transfer pathways and quantify their associated kinetics.

https://doi.org/10.1021/acs.jpcc.6c03692
J. Phys. Chem. C XXXX, XXX, XXX−XXX

Our analysis resolves field-induced dipole moment changes, energy-resolved electron and hole population dynamics, orbital-level contributions to photoexcitation, and the evolution of induced internal electric fields, while simultaneously elucidating both electron and hole transfer pathways involving the sacrificial agent and the Pt cocatalyst. By integrating electronic coupling strengths, energy-level alignments, and reorganization energies, we identify charge-transfer rates as a unifying and predictive descriptor that directly correlates with experimentally observed photocatalytic efficiencies, surpassing conventional metrics such as substituent size, electronegativity, or absorption strength. Specifically, our integrated workflow combines real-time time-dependent density functional theory (RT-TDDFT) to track ultrafast carrier dynamics, projection operator diabatization (POD) to extract parameter-free interfacial electronic couplings, and Marcus−Hush theory to quantify charge-transfer kinetics. Unlike studies employing these techniques in isolation, this multiscale integration establishes a direct physical link between early stage photoinduced exciton dynamics and macroscopic interfacial charge-extraction rates. In this way, the present study establishes a direct link between molecular-level excited-state processes and macroscopic catalytic performance. This unified molecular-level picture reveals how exciton migration, charge separation, and carrier redistribution collectively govern photocatalytic performance in COFs, providing a rational and transferable framework for designing next-generation photocatalysts with improved efficiency and stability.

2. COMPUTATIONAL METHODS

2.1. Ground-State Structure Optimization

To capture the essential structural and electronic features of the COF photocatalysts while maintaining computational feasibility, a molecular fragment comprising 77 atoms was extracted from the extended COF layer. This fragment was chosen to be sufficiently large to preserve the local chemical environment and conjugation relevant to photophysical processes. The optimized fragment structures, along with the corresponding periodic COF unit cells, are shown in Figure 1. Geometry optimizations of the molecular fragments were performed using Gaussian09[39] at the B3LYP/6−31+G(d,p) [LANL2DZ for Pt] level of theory.

To investigate interfacial charge transfer processes involving the cocatalyst and sacrificial agent, periodic calculations were performed on a double-layer COF model containing 270 atoms, with one layer directly adopted from ref 38. Ascorbic acid molecules and a Pt cluster were explicitly placed on the COF surface to model hole and electron transfer pathways, respectively. The final adsorption geometries of both the ascorbic acid and the Pt cluster were selected based on the lowest binding energies obtained from systematic evaluations of multiple adsorption sites on the COF surface. Geometry optimizations were performed using the `Quickstep` module of the CP2K package.[40,41] The exchange−correlation energy was described using the Perdew−Burke−Ernzerhof (PBE)[42,43] functional within the generalized gradient approximation (GGA),[44] and interlayer van der Waals interactions were accounted for using Grimme's DFT-D3 dispersion correction.[45] An auxiliary plane-wave cutoff of 400 Ry was used for the charge density expansion. Core electrons were treated using Goedecker−Teter−Hutter (GTH) pseudopotentials,[46,47] while valence electrons were described using the TZVP-MOLOPT-PBE-GTH basis set for all elements. To ensure smooth occupation near the Fermi level, Fermi−Dirac smearing corresponding to an electronic temperature of 298.15 K was applied.

2.2. Excited-State and Real-Time Electron Dynamics Simulations

Excited-state properties and ultrafast electron dynamics were investigated using real-time time-dependent density functional theory as implemented in the GPAW code[48,49] along with the atomic simulation environment (ASE).[50] RT-TDDFT calculations were carried out on the optimized 77-atom COF fragments in the linear combination of atomic orbitals (LCAO)[51] mode, employing the PBE exchange−correlation functional, a double-ζ polarized (DZP) basis set, and a real-space grid spacing of 0.2 Å. A minimum vacuum spacing of 6 Å was applied in all directions to eliminate spurious interactions arising from the finite simulation box. Photoabsorption spectra were obtained by applying a delta-kick perturbation of strength 0.514 mV/Å along the x direction, followed by real-time propagation for 3000 time steps with a time increment of 10 attoseconds per step.[52] The frequency-dependent absorption spectra were obtained by Fourier transforming the time-dependent dipole moment, using a Gaussian broadening of 0.07 eV to ensure spectral smoothness. While semilocal functionals like PBE lack long-range exact exchange, PBE-based RT-TDDFT remains a robust and computationally tractable standard for capturing dynamic electronic responses in large periodic frameworks.[52] In our calculations, the primary absorption peak at 2.81 eV (*vide infra*) aligns well with the experimental optical envelope (300−550 nm), confirming that the dominant $\pi \rightarrow \pi^*$ excitation is faithfully represented. Because all COF variants are evaluated under the same protocol, the relative trends in carrier dynamics and transient state populations remain self-consistent and reliable.

To probe excited-state electron dynamics at specific optical transitions, Gaussian-shaped laser pulses were applied at the dominant absorption maxima identified from the photoabsorption spectra. These simulations were analyzed using the Rhodent program[53,54] to extract time-dependent quantities. The Gaussian pulse had an amplitude of 0.514 mV/Å and was centered at 10 fs, ensuring that the system remained within the linear response regime.

2.3. Charge-Transfer Rate Calculations

Charge-transfer rates between the COF, sacrificial agent, and cocatalyst were evaluated using the projection operator diabatization approach. In this framework, the double-layer COF (structure from ref 38.) was treated as a single electronic block, while the ascorbic acid and Pt cluster were treated as separate blocks to determine the hole and electron transfer processes, respectively (Figure 1a,b).[14,55] To quantify the interfacial electronic couplings required for the Marcus−Hush kinetic evaluations, coupling matrix elements (J_E) were evaluated using the POD scheme implemented within the `ET_COUPLING` module of CP2K.[56] The POD approach block-diagonalizes the converged self-consistent Kohn−Sham Hamiltonian of the combined system to construct orthogonal, fragment-localized diabatic states. This scheme provides an efficient framework for quantifying charge-transfer matrix elements without artificial constraint biases, and has been widely benchmarked for donor−acceptor interfaces, adsorbate−surface interactions, and heterojunction systems[14,56−60] Rather than relying on two-state constrained DFT (CDFT) or

https://doi.org/10.1021/acs.jpcc.6c03692
J. Phys. Chem. C XXXX, XXX, XXX−XXX

unphysical frontier molecular orbital (FMO) overlap approximations, the POD formalism performs an algebraic diabatization by partitioning the full system's Kohn−Sham Hamiltonian into orthogonalized fragment subspaces representing the donor (COF framework) and acceptor (Pt_4 cocatalyst). By projecting the total system wave functions onto these localized fragment bases, the POD method constructs a multistate diabatic Hamiltonian matrix, in which off-diagonal blocks represent the electronic coupling elements between specific donor and acceptor states. This multistate projection avoids short-range orbital-mixing artifacts and enables energy-resolved mapping of coupling strengths across the electronic band manifold, directly identifying the predominant donor−acceptor state pairs driving interfacial electron and hole transfer.

Electronic structure calculations were performed utilizing a similar set of parameters as described above. Orbital energy levels and electronic coupling elements were extracted using the `ET_COUPLING` module within the `PROPERTIES` section of CP2K. A tetrahedral Pt_4 cluster was adopted to model the Pt cocatalyst surface, representing the smallest reported unit that retains the essential electronic characteristics while ensuring computational efficiency. Such small cluster models are well established in the literature for capturing the key interfacial charge-transfer physics in photocatalytic systems involving Pt and other metals.[61−64] Importantly, the Pt_4 model enables a systematic and consistent comparative analysis across different COF frameworks, while avoiding the additional complexity associated with extended metallic surfaces, without compromising the reliability of the underlying physical insights.

Reorganization energies were computed using the four-point method[65] as implemented in Gaussian09.[39] Geometry optimizations and single-point energy calculations were carried out for both neutral and charged states at their respective equilibrium geometries. The B3LYP/6−31+G(d,p) level of theory was used for ascorbic acid, while the Pt cluster was treated using the B3LYP functional in conjunction with the LANL2DZ basis set. To ensure computational consistency while accurately capturing distinct physical phenomena, electronic structure methods were partitioned by domain. Interfacial geometries, energy alignments (ΔE), and electronic couplings (J_E) for periodic COF systems were computed consistently at the PBE level using POD to avoid energy-scale mismatches between driving forces and couplings. Conversely, reorganization energies (λ) of isolated molecular/cluster acceptors were calculated using B3LYP to capture localized structural relaxation properly. Because this dual-functional protocol was applied uniformly across all functionalized variants, any systematic energy offsets cancel out, leaving the relative trends in charge-transfer kinetics robust.

The application of the B3LYP hybrid functional in the static Gaussian calculations is specifically tailored to evaluating ground-state equilibrium geometries, harmonic vibrational frequencies, and inner-sphere reorganization energies (λ) for the molecular subcomponents (Pt_4 cluster and sacrificial donor). Although range-separated hybrid functionals are conventionally preferred for describing long-range photo-induced charge-transfer excitations in conjugated organic networks, B3LYP provides an accurate and computationally robust framework for evaluating ground-state potential energy surfaces and local vibrational modes. Because these static calculations supply the structural and nuclear reorganization parameters for the subsequent Marcus−Hush kinetic model, applying B3LYP consistently across all functionalized derivatives ensures a reliable comparative baseline for the molecular fragments.

The electronic coupling elements, reorganization energies, density of states, and energy-level alignments were combined within the Marcus−Hush[66,67] formalism to compute charge-transfer rates for hole transfer from the COF to ascorbic acid and electron transfer from the COF to the Pt cluster simultaneously, as given by eq 1.

$$k = \frac{2\pi}{\hbar}\int J_E^2(E)\frac{1}{1+\exp\left(\frac{E-E_F}{kT}\right)}n(E)\frac{1}{\sqrt{4\pi\lambda kT}} \exp\left[-\frac{(\lambda-\Delta E+q\eta)^2}{4\lambda kT}\right]dE \quad (1)$$

Here, J_E denotes the electronic coupling between the COF states at energy E and the HOMO of the sacrificial agent (for hole transfer) or the LUMO of the Pt cocatalyst (for electron transfer). The quantity q is the elementary charge, and $n(E)$ represents the density of states at energy E. ΔE corresponds to the energy offset between E and the relevant HOMO/LUMO level of the sacrificial agent or Pt cluster, E_F is the Fermi level, λ is the reorganization energy, k is the Boltzmann constant, and T is the temperature, taken as 298.15 K. η is the overpotential of the system, which is taken to be 0. This corresponds to directly using the computed electronic energies without introducing any adjustable parameters. This approximation does not affect the relative trends in the calculated charge-transfer rates, as demonstrated in our earlier studies.[14,55] Since our objective is to establish a consistent, comparative framework across different COFs, using $\eta = 0$ avoids introducing system-dependent bias while preserving the observed correlation with experimental catalytic activity.

The POD-based approach for evaluating charge-transfer rates is well established and has been applied across a wide range of systems. For instance, Blumberger and co-workers have employed this methodology to investigate electron injection from dye molecules into TiO_2, as well as charge transfer from self-assembled monolayers (SAMs) to metallic Au surfaces.[56] This approach has also been extensively applied to organic semiconductor systems, where charge transfer between various electrode materials (Au/Ag/MoO_3) and organic polymers has been studied, showing a clear correlation between computed charge-transfer rates and experimentally measured contact resistances (R_C).[68] Furthermore, the method has been used to investigate charge-injection processes in organic field-effect transistors (OFETs), particularly at interfaces between interlayer-functionalized electrodes (IFEs) and OSCs, where the calculated rates correlate with the corresponding R_C values. Beyond organic systems, the POD approach has also been applied to perovskite materials; for example, Prezhdo et al. demonstrated charge transfer between interlayers in a two-dimensional perovskite system.[59] In addition, its applicability extends to photocatalytic systems, where it has been used to study interfacial charge-transfer processes relevant to catalytic activity.[14,55]

https://doi.org/10.1021/acs.jpcc.6c03692
J. Phys. Chem. C XXXX, XXX, XXX−XXX

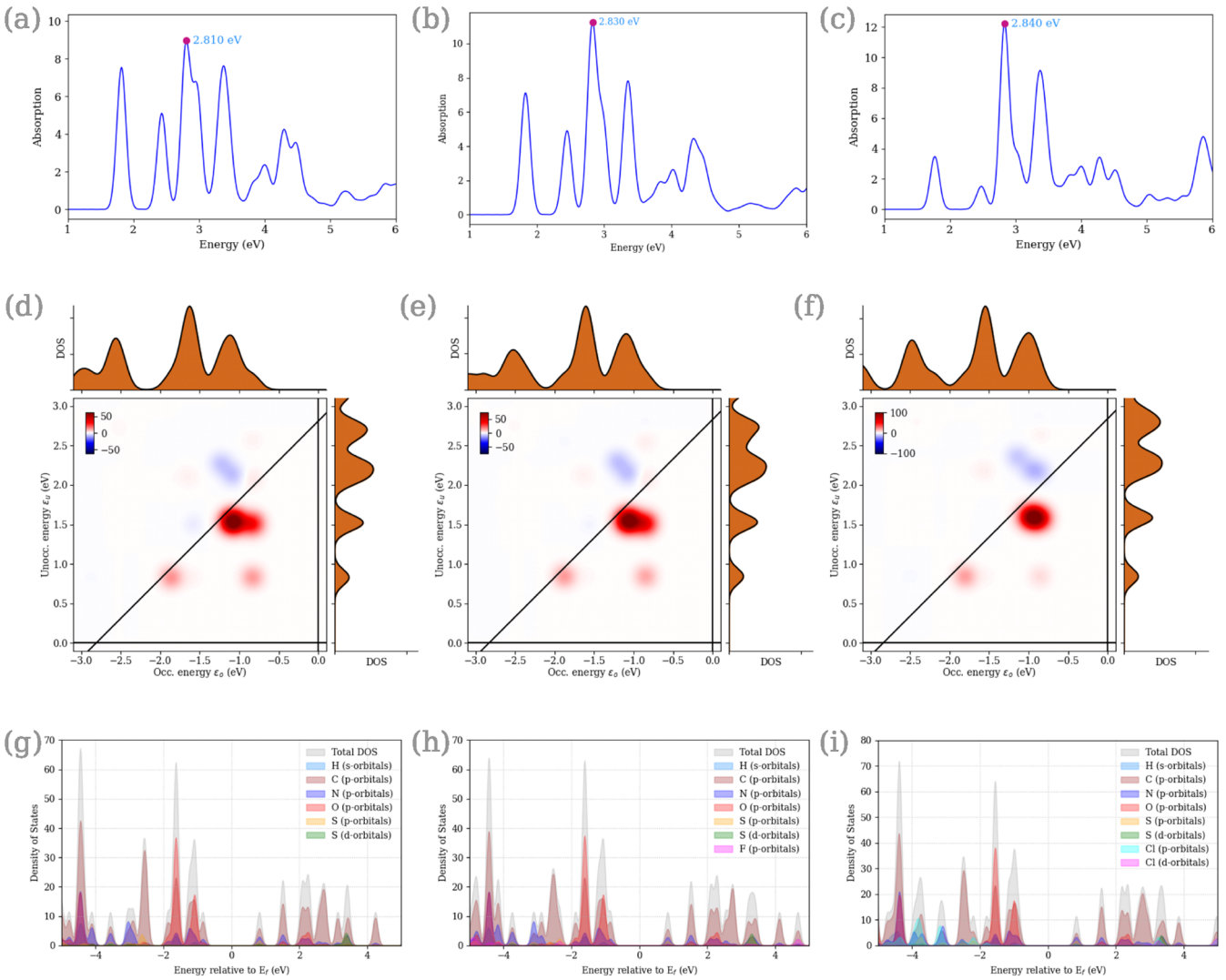

Figure 2. Excited-state characteristics of H−COF (a, d, g), F-COF (b, e, h), and Cl-COF (c, f, i). Top row: RT-TDDFT photoabsorption spectra highlighting the dominant low-energy excitonic band. Middle row: transition contribution maps (TCMs) illustrating the Kohn−Sham transitions contributing to the primary optical excitation. Bottom row: orbital-resolved density of states (DOS) showing elemental and angular momentum contributions near the Fermi level. Together, these analyses reveal a framework-centered $\pi-\pi^*$ exciton with substituent-tuned delocalization and transition mixing.

3. RESULTS AND DISCUSSION

3.1. Excited-State Photophysics and Exciton Structure in TP−Benzothiadiazole COFs

Having established the computational framework and charge-transfer formalism, we now turn to the electronic excited-state properties that govern photoinduced processes in these COFs. Because exciton formation, localization, and migration represent the earliest steps following light absorption—and ultimately determine the efficiency of subsequent interfacial charge separation—we first analyze the nature of the optical excitations and their orbital origins before progressing to charge-transfer coupling and kinetic rates.

The excited-state response is examined for three experimentally realized COFs sharing a common two-dimensional TP-benzothiadiazole (BT) backbone: the unsubstituted framework (H−COF) and its fluorine- and chlorine-substituted analogues (F-COF and Cl-COF). Halogen substitution at the meta position of the BT unit provides a controlled perturbation of the electronic structure without altering the underlying topology of the conjugated network. All excited-state analyses are performed on the optimized 77-atom fragments, which preserve the local donor−acceptor environment central to light absorption and charge redistribution. Figure 2 summarizes the key excited-state characteristics of the three COFs through their photoabsorption spectra, transition contribution maps (TCMs), and orbital-resolved densities of states (DOS). Despite chemical substitution, all three systems exhibit a common excitonic backbone dominated by transitions within the extended TP−BT framework, indicating that the primary photoactive motif remains intact across the series. Substituents modulate the detailed electronic structure near the frontier region, thereby tuning exciton composition rather than introducing fundamentally new optical transitions.

Photoabsorption Spectra. The photoabsorption spectra (top row of Figure 2) reveal a pronounced lowest-energy absorption band centered at approximately 2.8 eV for all three COFs, accompanied by weaker features spanning roughly 2.0−3.8 eV. The 0.07 eV Gaussian broadening applied to the calculated dipole power spectra is a numerical postprocessing

https://doi.org/10.1021/acs.jpcc.6c03692
J. Phys. Chem. C XXXX, XXX, XXX−XXX

parameter chosen to resolve fine electronic transition structures and pinpoint the dominant optical transition frequencies.[52] While experimental absorption spectra[38] exhibit broader, featureless bands due to thermal disorder, structural paracrystallinity, and environmental inhomogeneities, the computed excitation profile places the primary absorption maximum near 2.8 eV (∼443 nm), well within the experimental broad absorption band (300−550 nm). Applying a narrower numerical broadening ensures that the resonant excitation energy used to drive the real-time carrier propagation accurately targets the core dipole-allowed electronic transition of the functionalized framework.

The selection of the 2.8 eV (∼443 nm) optical pump frequency for the real-time TDDFT trajectory simulations is motivated by the need for a consistent excitation protocol across all functionalized variants. While a secondary absorption feature appears near 1.8 eV, its transition dipole moment varies considerably across the functionalized series, exhibiting marked intensity attenuation in the Cl-COF derivative (Figure 2c). In contrast, the 2.8 eV band corresponds to a robust, dipole-allowed charge-transfer transition present in all three frameworks, placing it comfortably within the experimentally observed solar light-harvesting window (300−550 nm). Exciting the systems at a uniform energy of 2.8 eV eliminates baseline-intensity artifacts, ensuring that differences in the observed charge-transfer dynamics directly reflect the intrinsic electronic influence of the functional groups rather than disparities in initial photon-absorption probability. The persistence of this dominant peak reflects the shared π-conjugated backbone, while subtle variations in peak shape and relative intensity arise from substituent-induced changes in the local electronic environment. Notably, halogenation does not lead to a significant red- or blue-shift of the main excitonic resonance, suggesting that substitution primarily affects transition mixing and the distribution of oscillator strengths rather than the overall optical gap.

Transition Contribution Maps and Exciton Character. Further insight into the nature of the optical excitations is obtained from the TCMs shown in the middle row of Figure 2. The x-axis represents the occupied states and the y-axis the unoccupied states of the COF, both referenced to the Fermi level. The total densities of states for the occupied and unoccupied manifolds are shown in brown along the corresponding parallel axes. The diagonal line denotes transitions at 2.8 eV. Red regions near the diagonal indicate constructive interference and thus positive contributions to exciton formation at this energy, whereas blue regions signify destructive interference. For all three COFs, the intense absorption near 2.8 eV originates from a relatively narrow cluster of Kohn−Sham transitions located close to the diagonal of the map, indicating that a limited number of occupied−unoccupied orbital pairs carry most of the oscillator strength. The concentration of red (constructive) features around states immediately below and above the Fermi level points to a well-defined excitonic transition rather than a highly delocalized superposition of many weak channels. Blue (destructive) regions in the vicinity reflect interference between energetically proximate π−π^* transitions. Comparison across the series reveals systematic differences in exciton delocalization. Cl-COF exhibits a more compact red region, consistent with a comparatively localized exciton dominated by a narrow set of frontier orbitals. In contrast, H−COF and F-COF display broader distributions of both constructive and destructive contributions, extending over a wider range of occupied and virtual states. This behavior indicates enhanced mixing among near-resonant transitions and a modest increase in excitonic delocalization along the framework upon halogen substitution. Notably, Cl-COF displays the most intense and compact red region among the three systems, with constructive contributions overwhelmingly dominating over the comparatively diffuse and spatially limited blue regions. This pronounced imbalance signifies a highly efficient utilization of incident photons for exciton generation, underscoring the superior antenna character of Cl-COF relative to its H- and F-substituted counterparts.

Orbital-Resolved DOS and Nature of the Optical Transition. The orbital-resolved DOS plots (bottom row of Figure 2) clarify the chemical origin of the states participating in these excitations. In all cases, the frontier region is dominated by C and N p-orbitals, with notable contributions from O p- and S p/d-states associated with the TP knots and BT linkers. Halogen p-states appear primarily deeper in the valence band or higher in the conduction band, contributing only indirectly to the frontier electronic structure. As a result, the lowest bright excitation can be consistently characterized as an intraframework π−π^* transition within the TP−BT network. The correspondence between DOS features near E_F and the TCM hot spots indicates that the occupied states involved in excitation are largely N/O-rich π-type orbitals, while the accepting unoccupied states have significant C/S-centered π^* character. This orbital alignment introduces an intralayer charge-transfer component within an otherwise strongly allowed π−π^* excitation. Importantly, the absence of localized halogen-derived or metal-like states near the Fermi level ensures that the bright exciton remains framework-centric, a feature favorable for in-plane exciton migration and subsequent coupling to interfacial charge-transfer pathways.

A more detailed inspection of the transition contribution maps reveals a particularly productive electronic channel connecting valence states centered around −1.0 eV to conduction states near +1.5 eV. While O p-orbitals contribute appreciably to the initial valence states, they are largely absent from the destination conduction manifold, indicating that the dominant constructive interference (red regions) arises from transitions that effectively displace electron density away from oxygen sites and into the conjugated C/N framework. This redistribution promotes enhanced charge delocalization across the π-conjugated backbone and underpins the strong oscillator strength of the excitation. In contrast, transitions originating from similar valence energies but terminating in higher-lying conduction states around +2.2 eV primarily contribute to destructive interference. These destination states recover significant O p-character, reintroducing localized electronic density that counteracts coherent charge flow. Consequently, the −1.0 eV → +1.5 eV transition can be viewed as an efficient "pump" that drives electrons from O-rich regions into O-poor, highly delocalized π^* states, whereas the −1.0 eV → +2.2 eV channel represents an electronically frustrated pathway. The re-emergence of oxygen character at higher conduction energies likely acts as an electronic bottleneck or symmetry-mismatched sink, suppressing the transition dipole and giving rise to the blue (negative) features observed in the maps.

Effect of Halogen Substitution. Halogen substitution subtly modifies the electronic landscape near the band edges without perturbing the underlying excitonic topology. A comparative analysis of the electronic structure shows that

https://doi.org/10.1021/acs.jpcc.6c03692
J. Phys. Chem. C XXXX, XXX, XXX−XXX

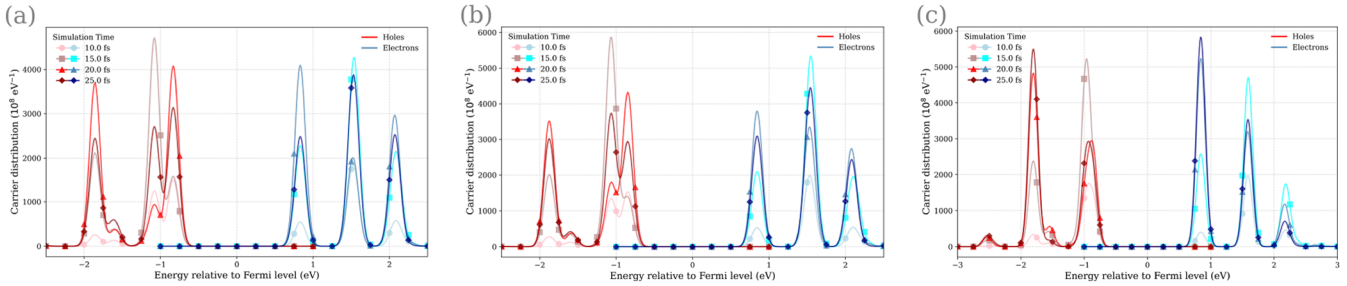

Figure 3. Ultrafast energy-resolved carrier dynamics following resonant excitation. Time-dependent distributions of hole and electron populations in (a) H−COF, (b) F-COF, and (c) Cl-COF fragments after Gaussian-pulse excitation at 2.8 eV. Carrier populations are shown at 10, 15, 20, and 25 fs, illustrating substituent-dependent charge separation and early time carrier redistribution on the COF surface.

fluorine 2*p* states are localized deep within the valence band (below −4 eV), whereas chlorine 3*p* states exhibit substantial density in the −2 to −5 eV range. This closer energetic alignment enables more effective hybridization with the *p*-orbitals of the COF framework. Notably, the unoccupied density of states (DOS) remains qualitatively similar across all three systems; however, the transition contribution map of the Cl-substituted COF displays a 2-fold increase in transition density, reaching a maximum value of 100 compared to 50 for both the F-substituted and parent systems (Figure 2d−f). This demonstrates that the enhanced optical response does not originate from an increased availability of unoccupied states, but rather from a pronounced amplification of the transition matrix elements. The higher polarizability and favorable energy alignment of the Cl 3p and 3d orbitals promote stronger electronic coupling between frontier orbitals, thereby significantly enhancing the oscillator strength of the dominant absorption features. However, whether this characteristic of Cl substitution is sufficient to yield superior efficiency compared to H−COF and F-COF remains to be investigated.

Taken together, the combined photoabsorption, TCM, and DOS analyses establish that the lowest-energy bright exciton in all three COFs is a framework-centered $\pi-\pi^*$ excitation with an embedded intraframework charge-transfer component. While halogen substitution does not qualitatively alter the nature of this excitation, it modulates the degree of exciton delocalization and frontier-orbital mixing. To assess how these differences manifest in the earliest stages of charge separation and early time carrier redistribution following photoexcitation, we next examine the ultrafast, energy-resolved carrier dynamics induced by resonant optical pumping.

Ultrafast Carrier Dynamics and Real-Space Charge Redistribution. The 30 fs real-time propagation window is designed to resolve the initial coherent electronic motion and early time carrier redistribution across the COF series immediately following resonant excitation.[52] Rather than modeling long-time thermalization or electron−phonon cooling dynamics, this time scale explicitly captures electronic decoherence, dynamic polarization, and nonequilibrium charge transfer across the functionalized framework variants. Figure 3 presents the time-dependent distributions of electron and hole populations in H-, F-, and Cl-COF fragments following Gaussian-pulse excitation at the dominant absorption maximum (∼2.8 eV) at times 10, 15, 20, and 25 fs of the 30 fs window. The temporal profile of the applied optical field and the corresponding induced dipole response, which directly reflect the light−matter interaction driving these dynamics, are shown in Figure S1. Across all three systems, the carrier populations exhibit a pronounced increase between 10 and 15 fs, coinciding with the temporal maximum of the laser pulse, followed by partial redistribution over a broader energy window by 20−25 fs. In Cl-COF, holes redistribute into states substantially deeper below the Fermi level than the energies accessed by electrons above it, reflecting an intrinsically asymmetric early time carrier redistribution in which holes populate lower-energy valence-band states more readily. In contrast, electrons—particularly in the H- and F-substituted frameworks—remain distributed over higher-energy conduction-band states during the simulated time window, indicating a slower redistribution of the excited electron population. The transient presence of hot carriers at energies exceeding ±2 eV highlights the multistep nature of exciton dissociation and the subsequent early time carrier redistribution in these extended π-conjugated frameworks.

Apparent substituent-dependent differences emerge in the energy-resolved carrier distributions, particularly at later times ($t \approx 25$ fs), where distinct carrier redistribution patterns can be resolved. In H−COF (Figure 3a), the maximum hole population is centered near −1.1 eV, while electrons peak around 1.6 eV, indicating partial redistribution of the photoexcited carriers but noticeable carrier stagnation in intermediate conduction states. A similar behavior is observed for F-COF (Figure 3b), where electrons also remain predominantly trapped near +1.6 eV despite the availability of lower-lying conduction states. In contrast, Cl-COF (Figure 3c) exhibits a markedly different behavior: electrons become preferentially redistributed into the lowest conduction state near +0.8 eV, while the populations of higher-energy conduction states are comparatively reduced. This population redistribution suggests a more efficient occupation of lower-energy conduction-band states in the chlorine-substituted framework during the simulated time window. The hole dynamics further accentuate this distinction. In both H- and F-COFs, the hole population remains broadly distributed across three energetic regions centered at approximately −0.8, −1.1, and −1.8 eV, reflecting a broader early time redistribution of holes within the valence band. Conversely, Cl-COF simplifies this landscape into two dominant hole populations near −0.9 and −1.8 eV, effectively eliminating the intermediate −1.1 eV channel. By concentrating the highest hole density in the deepest valence state, chlorine substitution stabilizes charge separation and establishes a more energetically favorable configuration for downstream interfacial hole transfer. However, despite the favorable energetics, it remains to be determined whether this effect manifests as a measurable enhancement in photocatalytic efficiency.

The relative magnitudes of the simulated peak carrier densities follow the trend H−COF < Cl-COF ≈ F-COF, with

https://doi.org/10.1021/acs.jpcc.6c03692
J. Phys. Chem. C XXXX, XXX, XXX−XXX

F- and Cl-substituted frameworks reaching peak values of ~6000 × 10^{-8} eV^{-1}, compared to ~4000−5000 × 10^{-8} eV^{-1} for H−COF. The computed enhancement in transient carrier density upon halogenation directly aligns with experimentally measured average excited-state lifetimes for the periodic frameworks, which increase from 1.69 ns in H−COF to 1.94 ns in Cl-COF and reach a maximum of 2.84 ns in F-COF. While early time RT-TDDFT simulations reflect the instantaneous electronic response during the initial optical pulse ($\lesssim$ 100 fs)—where fluorine and chlorine substituents induce comparable electronic polarization (Cl−COF ≈ F−COF)—the nanosecond-scale experimental lifetimes are influenced by additional nuclear relaxation channels. Specifically, the slightly shorter lifetime of Cl-COF relative to F-COF in experimental measurements originates from long-time heavy-atom spin−orbit effects and enhanced nonradiative vibrational quenching, which are active on the nanosecond time scale but fall outside the early time electronic-propagation window of frozen-nuclei RT-TDDFT trajectory calculations. The higher transient carrier densities in the halogen-substituted systems therefore reflect slower geminate recombination and enhanced stabilization of charge-separated states, consistent with the electron-withdrawing nature of fluorine and, to a lesser extent, chlorine. From a photocatalytic perspective, these substituent-dependent carrier redistribution dynamics have direct mechanistic implications. The accumulation of holes in deep valence states (~−1.8 eV) in Cl-COF implies a stronger oxidizing potential, favoring efficient hole transfer to sacrificial donors. In contrast, the persistence of higher-energy electrons around +1.6 eV in H- and, especially, in F-COF provides a larger reductive overpotential, enhancing the driving force for electron transfer to the Pt cocatalyst during proton reduction. When viewed alongside the TCM and DOS analyses, these results demonstrate how subtle modifications in excitonic structure and ultrafast carrier dynamics translate into measurable differences in charge separation yields and interfacial charge-transfer kinetics. This dynamic picture provides a critical bridge between excited-state photophysics and the POD-derived electronic couplings and Marcus−Hush rate analyses discussed in the following section.

To complement the energy-resolved carrier populations discussed above, we next examine the real-space evolution of the photoinduced charge density, which provides a direct visualization of how the initially generated carriers redistribute across the framework on ultrafast time scales. Figure 4 shows the induced charge density difference, $\Delta\rho$, for F-COF following resonant excitation at 2.8 eV, with green and pink isosurfaces denoting regions of electron accumulation and depletion, respectively. At early times (10 fs), the induced density exhibits pronounced charge separation across the molecular fragment, with accumulation and depletion localized at opposite termini, while the central node displays an alternating pattern of charge rearrangement. This spatial organization reflects the framework-centered $\pi-\pi^*$ excitation with embedded intraframework charge-transfer character, as identified from photoabsorption, TCM, and DOS analyses. Between 10 and 15 fs, an apparent inversion of electronic polarity is observed throughout the fragment, signaling coherent charge oscillation along the conjugated backbone. The large spatial extent of the isosurfaces at these time steps indicates substantial carrier delocalization, consistent with the presence of hot, mobile carriers inferred from the energy-

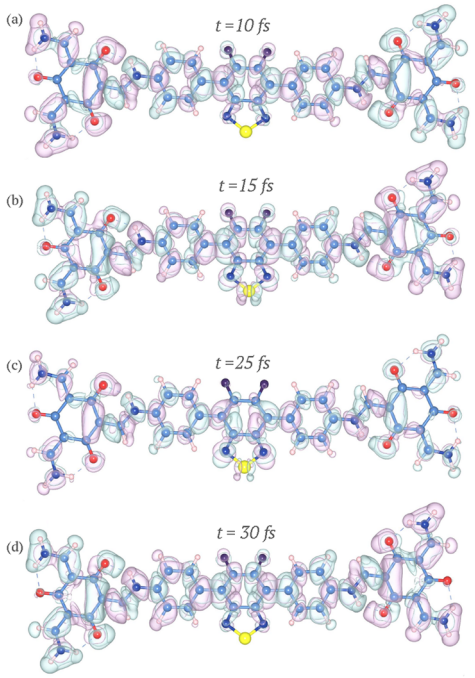

Figure 4. Ultrafast evolution of photoinduced charge density in F-COF. Induced charge density difference ($\Delta\rho$) following 2.8 eV Gaussian-pulse excitation at (a) 10 fs, (b) 15 fs, (c) 25 fs, and (d) 30 fs. Green and pink isosurfaces represent regions of electron accumulation and depletion, respectively, highlighting the spatial evolution of photoinduced charge redistribution following excitation.

resolved distributions. By 25 fs, the induced charge density undergoes a further polarity reversal accompanied by a marked contraction of the isosurfaces, indicating transient charge localization and partial damping of the coherent motion. This behavior aligns with the redistribution of carriers toward lower absolute energies observed in the time-resolved carrier distributions. At later times (30 fs), the charge density re-expands and shifts directionally, suggesting the onset of slower, incoherent transport regimes following the decay of the initial coherent dynamics. Importantly, analogous spatiotemporal charge-density oscillations and polarity inversions are also observed for H−COF and Cl-COF, as shown in Figures S2 and S3, although with reduced spatial extent and more rapid damping compared to F-COF. These trends are consistent with the substituent-dependent carrier lifetimes and separation efficiencies discussed above, reinforcing the conclusion that fluorine substitution enhances delocalization and stabilizes charge-separated configurations on ultrafast time scales.

The rapid, oscillatory charge density redistributions observed across the donor fragments within the initial 30 fs window reflect coherent quantum beats driven by electronic superpositions in the photoexcited state. In our finite molecular models, these oscillations illustrate the strong local electronic coupling between adjacent structural units. In an extended 2D COF lattice with periodic π-conjugation, such early time electronic coherence acts as the initial stage of spatial charge migration, where coupling to framework vibrational modes breaks phase coherence and converts local charge oscillations into directed, long-range carrier separation across the porous framework.

The selection of the cluster model is motivated by the need to unambiguously isolate the intrinsic donor−acceptor photo-

https://doi.org/10.1021/acs.jpcc.6c03692
J. Phys. Chem. C XXXX, XXX, XXX−XXX

excitation pathways and evaluate localized electronic coupling elements within a computationally tractable fragment framework. In the extended 2D COF lattice, each central TP node is covalently bonded to three electron-withdrawing BT units, creating a more electron-deficient donor core in the ground state compared to isolated oligomeric fragments. This 3-fold acceptor functionalization enhances intraframework polarization, leading to a moderate red-shift in the charge-transfer absorption onset and an elevated transition dipole moment without altering the fundamental orbital symmetry or the relative substituent-dependent trends across the functionalized series.

In addition to intramolecular connectivity, macroscopic environmental factors—specifically interlayer $\pi-\pi$ stacking and solvent dielectric response—further tune the absolute energies of intrasheet charge-transfer states. Interlayer interactions in the bulk periodic COF facilitate spatial charge delocalization along the stacking axis, which stabilizes charge-transfer intermediates relative to gas-phase cluster models. Similarly, polar solvent environments offer dielectric screening that lowers exciton binding energies and stabilizes polar excited-state configurations, thereby promoting efficient charge separation prior to interfacial electron transfer.

While the present RT-TDDFT analysis focuses on real-space charge density differences, transition contribution maps, and energy-resolved carrier occupations to capture interfacial charge dynamics, time-resolved population tracking projected onto individual subcomponents (such as TP vs BT units) can offer a complementary view of intraframework charge oscillations. Although explicitly partitioning transient populations across individual chemical fragments is beyond the scope of this work, the observed dynamic polarization patterns clearly illustrate how halogen substitution influences the initial spatial distribution and interfacial migration of photoexcited carriers.

Collectively, the induced charge-density dynamics provide a real-space counterpart to the energy-resolved carrier analysis, demonstrating how subtle differences in excitonic structure and carrier redistribution dynamics translate into distinct patterns of coherent charge motion and localization. This unified picture of excited-state evolution establishes the mechanistic foundation for the subsequent POD analysis, where these transient charge distributions are mapped onto interfacial electronic couplings and charge-transfer rates relevant to photocatalytic hydrogen evolution.

3.2. Interfacial Binding and Electronic Coupling Framework

Having established how halogen substitution modulates exciton structure, early time excited-state dynamics, and real-space charge redistribution, we now turn to the interfacial processes that ultimately govern photocatalytic activity. In these COF-based systems, hydrogen evolution proceeds via spatially separated redox half-reactions, requiring efficient extraction of photogenerated electrons and holes at distinct interfaces. Quantifying the electronic coupling at these interfaces is therefore essential for connecting excited-state dynamics to experimentally measured hydrogen evolution rates. Experimentally, all three parent COFs (H-, F-, and Cl-COF) have been shown to catalyze hydrogen evolution under visible-light irradiation in the presence of a sacrificial hole scavenger (ascorbic acid) and a Pt cocatalyst. Upon photoexcitation, electrons promoted to the conduction band migrate toward the Pt surface, where proton reduction occurs, while valence-band holes are rapidly quenched by oxidation of ascorbic acid. This spatial separation suppresses geminate recombination, enabling sustained catalytic turnover. Building on this mechanistic picture, we employ the projected orbital density formalism to explicitly quantify both hole- and electron-transfer pathways, thereby directly correlating the computed charge-transfer rates with experimentally reported hydrogen production yields.

Before evaluating electronic couplings and transfer rates, it is necessary to characterize the thermodynamic affinity of the relevant interfaces, as binding strength directly influences orbital overlap and interfacial electronic structure. For this purpose, POD calculations were performed using a double-layer COF model containing 270 atoms, constructed by stacking the experimentally reported 135-atom monolayer along the out-of-plane direction (Figure 1b,c). A tetrahedral Pt nanocluster was adopted to represent the cocatalyst, and ascorbic acid was used as the hole scavenger, consistent with experimental conditions. The periodic COF−Pt_4 interfaces were treated in a closed-shell singlet spin multiplicity ($M = 1$, $S = 0$). Because the spin state and geometry of the Pt_4 cocatalyst were held strictly constant across all periodic COF systems, any spin-dependent electronic shifts act as a uniform baseline throughout the series, ensuring that the relative trends in POD-derived electronic couplings (J_E) and interfacial charge-transfer rates (k_{et}) remain self-consistent and robust.

The calculated binding energies of ascorbic acid and Pt on the various COF surfaces are summarized in Table 1. Among

Table 1. Binding Energies (E_B, in eV) of Ascorbic Acid (Hole Scavenger) and Pt Nanocluster (Electron Cocatalyst) Adsorbed on Substituted COF Surfaces, Calculated Using the Double-Layer COF Model Employed for POD Analysis

Substitution	E_B, Pt	E_B, acid
−H	−2.69	−0.20
−F	−3.13	−0.23
−Cl	−2.45	−0.15
−Br	−2.52	−0.20
−CN	−2.66	−0.16
$-NO_2$	−2.75	−0.15
−COOH	−2.78	−0.17

the halogen-substituted systems, F-COF exhibits the strongest binding for both species. This behavior can be attributed to the high electronegativity of fluorine, which lowers the local frontier orbital energies and enhances interfacial polarization. The resulting increase in dipole−dipole interactions strengthens hydrogen bonding with ascorbic acid and facilitates electronic communication with the Pt cocatalyst. In contrast, Cl-COF shows the weakest binding, consistent with the larger atomic radius of chlorine, which limits close contact between the adsorbates and the COF surface and reduces effective orbital overlap. Extending this analysis to hypothetical functionalizations reveals that strongly electron-withdrawing and polar groups such as −CN, $-NO_2$, and −COOH substantially enhance the binding of ascorbic acid. The increased polarity of these substituents stabilizes interfacial hydrogen bonding, suggesting favorable conditions for hole extraction. While binding alone does not determine catalytic performance, these trends establish a critical energetic baseline for interpreting the POD-derived electronic couplings and subsequent Marcus−Hush charge-transfer rates.

https://doi.org/10.1021/acs.jpcc.6c03692
J. Phys. Chem. C XXXX, XXX, XXX−XXX

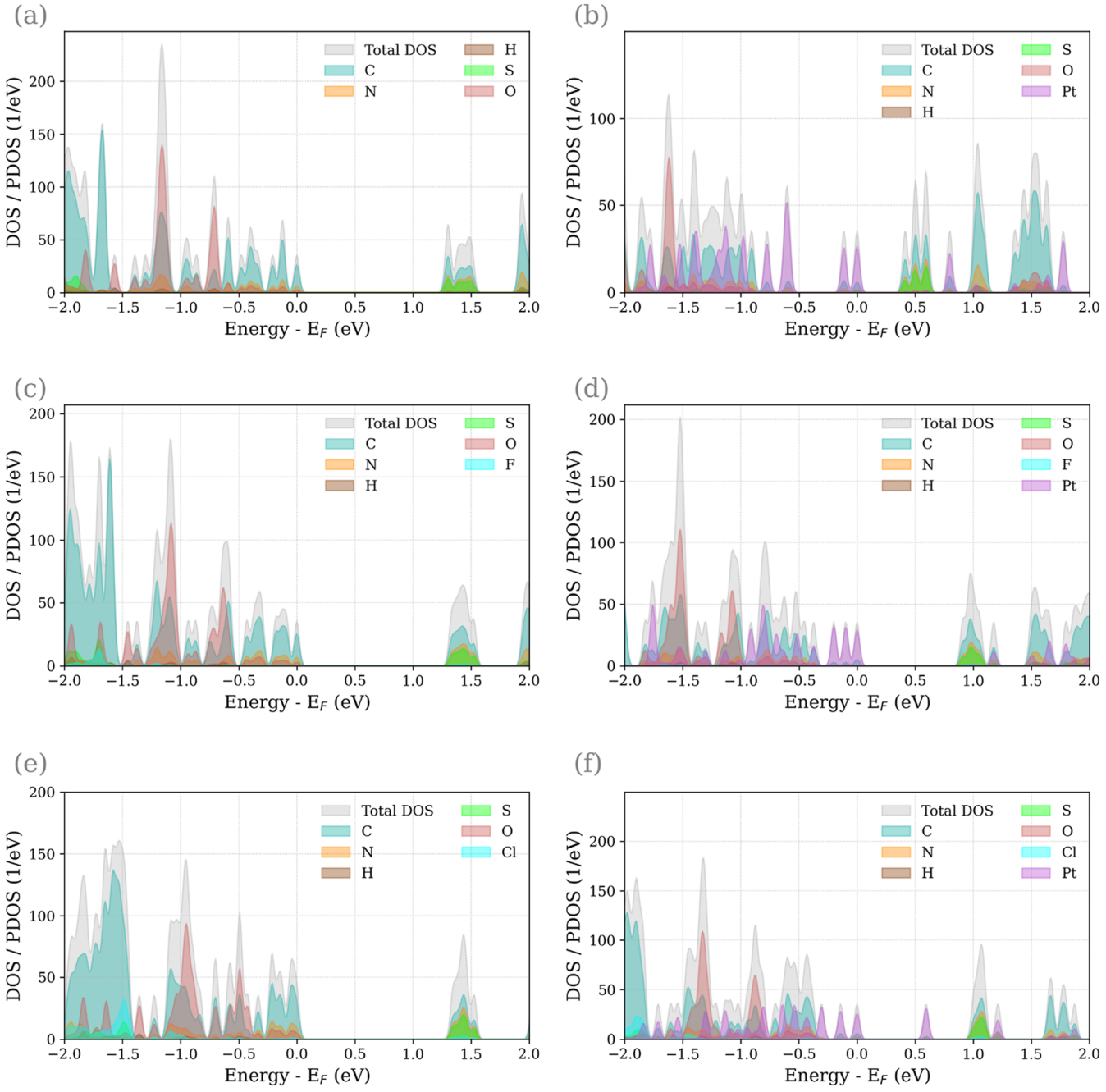

Figure 5. Projected density of states (PDOS) for acid−COF (a, c, e) and Pt−COF (b, d, f) interfaces in H-, F-, and Cl-substituted systems. Rows correspond to H−COF (top), F-COF (middle), and Cl-COF (bottom). The PDOS highlights the energetic alignment and hybridization between COF framework states and adsorbate- or Pt-derived orbitals near the Fermi level.

The interfacial binding geometries and corresponding adsorption energies (E_B) were computed for the Pt_4 cluster and the sacrificial donor in the absence of solvent to isolate the intrinsic electronic interactions across the various functionalized COF frameworks. In an experimental photocatalytic system, the presence of a protic aqueous solvent heavily influences interfacial adsorption through competitive hydrogen bonding and dielectric screening. Furthermore, the aqueous medium promotes the deprotonation of ascorbic acid to ascorbate anions, which increases local charge density and strengthens electrostatic binding to functionalized pore walls relative to neutral gas-phase species. Treating these interfaces without the solvent isolates the framework's native electronic influence, enabling a direct, comparative assessment of substituent effects on cocatalyst anchoring and donor binding, free from solvent-dependent structural fluctuations.

While this section targets the heterogeneous donor−COF−catalyst interface, interlayer $\pi-\pi$ stacking within the bulk COF material represents an additional structural dimension. Interlayer interactions govern the structural rigidity and channel alignment of the 2D framework, but the primary focus of this investigation remains on the local interfacial binding and electronic coupling pathways that dictate charge transfer to the cocatalyst and sacrificial species. The gas-phase binding metrics reported herein thus provide a clear baseline for evaluating how chemical modification alters intrinsic

https://doi.org/10.1021/acs.jpcc.6c03692
J. Phys. Chem. C XXXX, XXX, XXX−XXX

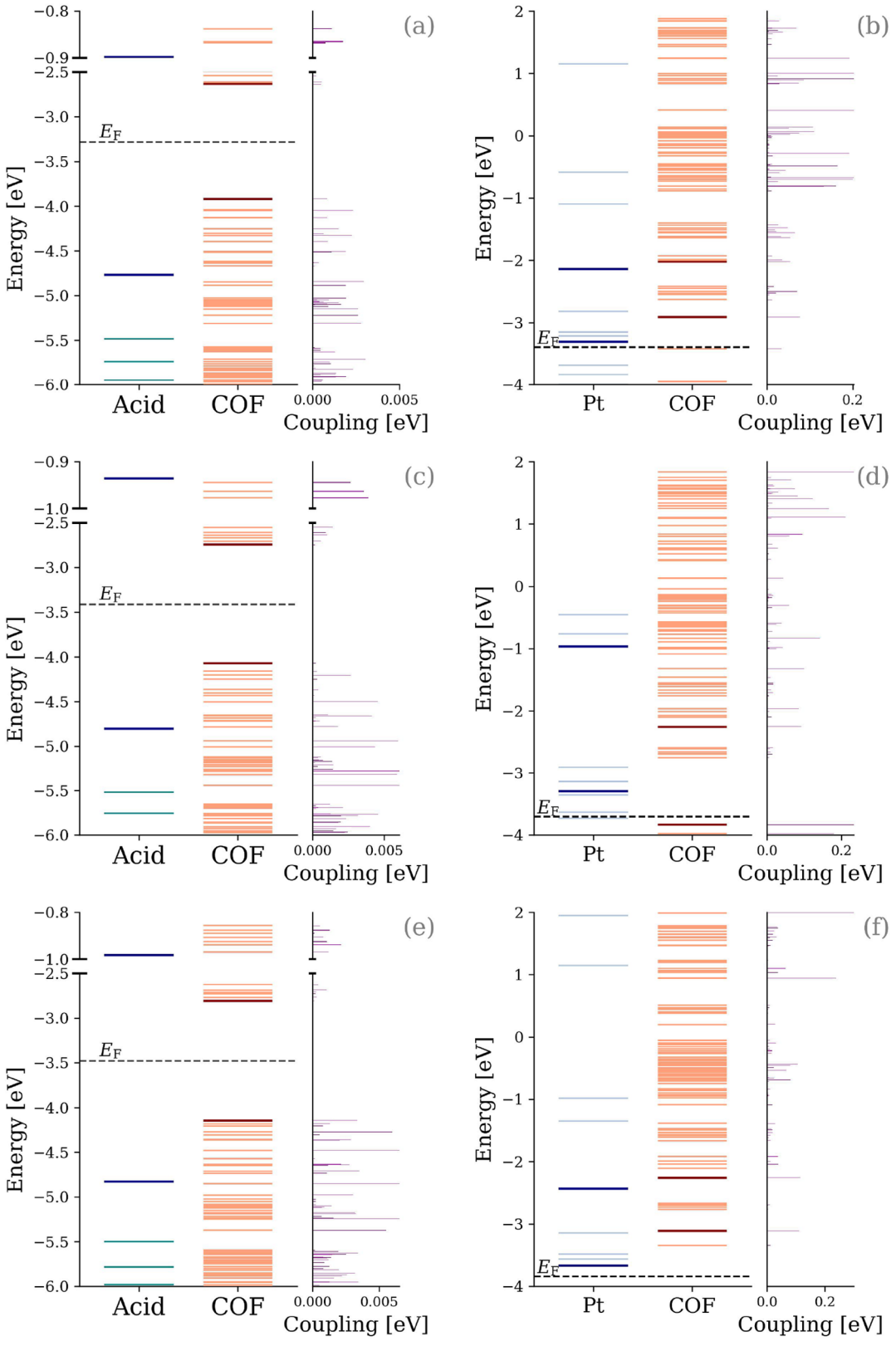

Figure 6. POD-derived frontier energy alignment and electronic couplings at the acid−COF (a, c, e) and Pt−COF (b, d, f) interfaces for H- (a, b), F- (c, d), and Cl- (e, f) substituted COFs, respectively. Acid and Pt energy levels are shown in teal and gray, respectively; blue lines represent HOMO and LUMO. COF states are indicated in orange; maroon lines show the VBM and CBM. Magenta bars represent energy-resolved electronic coupling elements between the acid HOMO or Pt LUMO and COF states. The black dashed line marks the Fermi level E_F. Data for additional functionalizations are provided in Figures S4 and S5.

https://doi.org/10.1021/acs.jpcc.6c03692
J. Phys. Chem. C XXXX, XXX, XXX−XXX

interface energetics prior to solvation and deprotonation events.

Although binding energetics establish the thermodynamic affinity of the acid−COF and Pt−COF interfaces, efficient charge extraction additionally requires favorable energetic alignment and orbital hybridization at the interface. To assess this electronic prerequisite, we analyze the projected density of states (PDOS) for the acid−COF and Pt−COF complexes, as shown in Figure 5. Across all H-, F-, and Cl-substituted systems, the states in the immediate vicinity of the Fermi level remain dominated by the conjugated COF backbone, with primary contributions from C, N, and O *p*-orbitals. Importantly, adsorption of either ascorbic acid or the Pt nanocluster does not introduce isolated midgap or deep trap states. Instead, adsorbate- and Pt-derived contributions appear as energetically overlapping features that hybridize with the intrinsic COF electronic manifold. For the acid−COF interfaces (Figure 5a,c,e), the O-centered states of ascorbic acid—and, where applicable, halogen-associated contributions—align with the upper valence-band region of the COF. This alignment creates a quasi-continuum of accepting states for photogenerated holes, enabling efficient hole extraction without carrier trapping. The enhanced overlap observed for more polar substitutions is consistent with their stronger binding energies and supports the role of interfacial polarity in stabilizing hole-transfer channels. In the Pt−COF complexes (Figure 5b,d,f), Pt-derived states overlap with the COF conduction-band edge, particularly in the F- and Cl-substituted systems. This energetic matching indicates a finite degree of electronic hybridization between the Pt and COF states, providing a direct pathway for electron injection into the cocatalyst. The increased DOS overlap for F-COF mirrors its stronger Pt binding and foreshadows the larger electronic couplings quantified in the subsequent POD analysis. Taken together, the PDOS results confirm that interfacial adsorption preserves the framework-centered electronic structure while enabling energetically well-matched, hybridized donor−acceptor states for both hole and electron extraction.

Building on the interfacial binding energetics and PDOS analysis, we next employ the POD framework to explicitly quantify how the energetic alignment and electronic coupling between the COF, sacrificial donor, and cocatalyst govern interfacial charge extraction. Figure 6 summarizes the POD-derived frontier energy levels and energy-resolved coupling strengths for the acid−COF and Pt−COF interfaces in H-, F-, and Cl-substituted systems. For the acid−COF interfaces (Figure 6a,c,e), the HOMO of ascorbic acid lies slightly deeper than the COF valence-band maximum in all three systems, establishing a thermodynamically favorable driving force for hole transfer from the photoexcited COF into the sacrificial donor. Beyond this energetic criterion, the POD analysis reveals pronounced substituent-dependent differences in electronic coupling. In F-COF, and to a lesser extent in Cl-COF, the acid HOMO exhibits stronger and more broadly distributed couplings to COF valence states near the VBM than in H−COF. The increased density and magnitude of these coupling elements result in a larger integrated coupling strength, consistent with the enhanced acid binding and favorable valence-band alignment inferred from the PDOS analysis. These features collectively indicate more efficient hole-extraction pathways in the halogen-substituted frameworks.

A complementary picture emerges at the Pt−COF interfaces (Figure 6b,d,f), where the relative alignment of COF conduction states and Pt acceptor levels governs electron extraction. For the H- and Cl-substituted frameworks, the Pt-derived LUMO manifold lies at or slightly below the COF conduction-band minimum, enabling photogenerated electrons to relax efficiently into the metallic acceptor states. In these systems, the Fermi level of the combined interface lies within the Pt-dominated electronic manifold rather than within the intrinsic COF gap, indicating effective Fermi-level pinning by the Pt cluster. In contrast, F-COF deviates from this behavior: the Pt acceptor levels are shifted relative to the COF conduction edge, leading to a less favorable energetic overlap and a departure from conventional pinning behavior. Despite this energetic distinction, F-COF exhibits both stronger and more numerous electronic coupling (J_E) elements between Pt acceptor states and COF conduction states, with Cl-COF displaying intermediate coupling strengths and H−COF the weakest overall interaction. This combination of altered level alignment and enhanced coupling highlights a distinct electron-transfer regime for F-COF, in which interfacial kinetics are more strongly governed by coupling strength than by simple energetic alignment.

Taken together, the POD analysis demonstrates that halogen substitution—most notably fluorination—simultaneously enhances hole-transfer coupling at the acid−COF interface and electron-transfer coupling at the Pt−COF interface. This dual optimization provides a microscopic, rate-relevant explanation for the superior photocatalytic performance of F-COF and the intermediate activity of Cl-COF relative to the unsubstituted framework. The resulting energetic alignments and POD-derived electronic couplings, together with the corresponding reorganization energies, constitute the complete set of microscopic inputs required for a quantitative evaluation of interfacial charge-transfer kinetics within the Marcus−Hush formalism. Using these parameters, we compute both hole-transfer rates from the COF to the sacrificial donor and electron-transfer rates from the COF to the Pt cocatalyst under zero overpotential conditions (eq 1). The electron-transfer rate constants were evaluated under a zero-overpotential reference condition (η = 0), corresponding to the intrinsic charge-transfer barrier where the thermodynamic driving force is zero. While practical photocatalytic conditions involve finite operating overpotentials that alter absolute kinetic rates, adopting a common η = 0 baseline allows for an unbiased comparative assessment of how halogen functionalization intrinsically modulates electronic coupling (J_E) and reorganization energy (λ).[68] Consequently, the relative kinetic trends across the H-, F-, and Cl-COF series remain self-consistent and representative of intrinsic material properties. The calculated rates are summarized in Table 2 and directly compared with experimentally reported hydrogen evolution rates in Figure 7.

A clear, systematic correlation emerges between the calculated hole-transfer rates and the experimental hydrogen-evolution activity for the three experimentally realized COFs. Among the halogen-substituted systems, F-COF exhibits the highest hole-transfer rate, followed by Cl-COF and then H−COF. This ordering mirrors the experimentally observed hydrogen production efficiencies, suggesting that hole extraction by the sacrificial donor is the key differentiating charge-transfer process governing the observed photocatalytic trend. The enhanced hole-transfer rate in F-COF directly

https://doi.org/10.1021/acs.jpcc.6c03692
J. Phys. Chem. C XXXX, XXX, XXX−XXX

Table 2. Calculated Marcus–Hush Hole-Transfer Rates (k_{ht}) from COF to Ascorbic Acid and Electron-Transfer Rates (k_{et}) from COF to Pt Cocatalyst[a]

Substitution	k_{ht} (s^{-1})	k_{et} (s^{-1})
–H	4.13×10^{11}	1.63×10^{10}
–F	3.30×10^{12}	1.16×10^{14}
–Cl	1.84×10^{12}	1.64×10^{10}
–Br	1.64×10^{12}	1.89×10^{10}
–CN	2.14×10^{12}	7.65×10^{12}
$-NO_2$	2.23×10^{12}	1.25×10^{13}
–COOH	1.95×10^{12}	1.59×10^{13}

[a]Reorganization energy for acid (λ_h) is 0.653 eV, while for Pt (λ_e) it is 0.604 eV. All rates are reported at zero overpotential.

reflects the combined effects of stronger acid binding, favorable valence-band alignment, and increased POD-derived electronic couplings discussed in the preceding sections.

Electron-transfer rates from the COF to the Pt cocatalyst display a sharply differentiated substituent dependence when examined alongside the corresponding hole-transfer rates. While hole-transfer kinetics increase progressively from H to Cl and reach a maximum for F, the electron-transfer rates exhibit far greater selectivity. In particular, F-COF exhibits an electron-transfer rate of 1.16×10^{14} s^{-1}, which is nearly 4 orders of magnitude larger than those of both H–COF (1.63×10^{10} s^{-1}) and Cl-COF (1.64×10^{10} s^{-1}). In contrast, the electron-transfer rates of H- and Cl-substituted frameworks are essentially indistinguishable, indicating that chlorination does not significantly improve electron extraction relative to the unsubstituted COF. This pronounced enhancement in F-COF is entirely consistent with the POD analysis, which identified substantially stronger and denser electronic couplings between COF conduction states and the Pt LUMO in the fluorinated system. When hole and electron transfer rates are considered together, F-COF clearly emerges as the most efficient photocatalyst, while Cl-COF offers only a moderate improvement in hole transfer without a corresponding gain in electron extraction, thereby reproducing the experimentally observed hierarchy of hydrogen evolution activity.

To further rationalize these observations, it is important to note that the computed charge-transfer rates for holes (Figure 7a) lie in the range of 10^{11}–10^{12} s^{-1}, whereas those for electrons (Figure 7b) span a significantly broader range of 10^{10}–10^{14} s^{-1}. This difference in both magnitude and spread arises from the fundamentally distinct nature of the two interfaces. Hole transfer from the COF to ascorbic acid occurs within a relatively uniform donor–acceptor environment, leading to a narrow distribution of electronic couplings and driving forces and, consequently, a confined range of rates. In contrast, electron transfer from the COF to the Pt cocatalyst is highly sensitive to the local interfacial configuration. Variations in COF–Pt distance, contact geometry, and the site-dependent electronic structure of Pt introduce substantial heterogeneity, which, within the Marcus formalism, translates into a wide distribution of electronic couplings and energy alignments, and hence a broader range of rate constants.

Differences in energy-level alignment further reinforce this distinction. The hole-transfer process is governed by the energy offset between the COF valence band maximum (VBM) and the HOMO level of ascorbic acid, which remains relatively invariant across the series. In contrast, the electron-transfer process depends on the alignment between the COF conduction band minimum (CBM) and the acceptor levels of the Pt cocatalyst, which vary more significantly due to interfacial structural heterogeneity. In combination with relatively strong electronic couplings (up to ~ 0.2 eV for H- and F-substituted systems), these variations amplify the spread in electron-transfer rates. Consequently, it is not expected that hole- and electron-transfer processes occur on the same time scale, as they are governed by distinct donor–acceptor interactions, coupling strengths, and interfacial energetics. The observed differences in rate magnitudes are therefore a natural outcome of the underlying physical processes rather than an inconsistency in the calculations. Importantly, Figure 7 is intended to highlight trends in correlation with experimental catalytic efficiency across the COF series, rather than to enable direct absolute comparison between panels. The consistent correspondence between the computed charge-transfer rates and experimentally reported hydrogen evolution activities suggests that these rates can serve as a physically meaningful

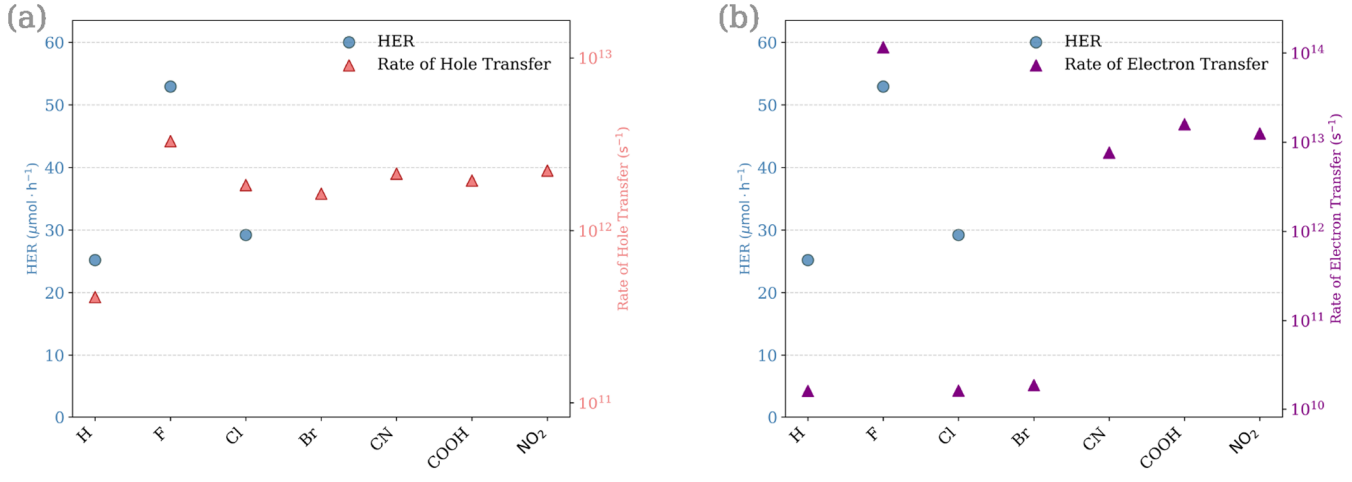

Figure 7. Correlation between calculated Marcus–Hush charge-transfer rates, using our theoretical framework and experimentally reported hydrogen evolution rates (HER), taken from ref 38. for different COF systems. (a) Hole-transfer rates from COF to ascorbic acid (pink triangles) compared with hydrogen evolution rates (steelblue circles). (b) Electron-transfer rates from COF to the Pt cocatalyst (purple triangles), compared with hydrogen evolution rates (steelblue circles).

https://doi.org/10.1021/acs.jpcc.6c03692
J. Phys. Chem. C XXXX, XXX, XXX–XXX

descriptor, and in principle, a predictive metric for screening photocatalytic COFs.

While the calculated interfacial electron-transfer rates (k_{et}) remain nearly invariant between H−COF and Cl-COF, the hole-transfer rates (k_{ht}) exhibit a strong dependence on halogen functionalization that aligns with the experimental photocatalytic hydrogen evolution activity. This sensitivity indicates that while electron transfer to the cocatalyst is kinetically facile across the series, efficient hole extraction serves as the primary differentiating factor governing overall carrier collection and recombination kinetics, rather than a strictly assigned single rate-determining step.

To clarify the spatial origin of the coupling matrix elements evaluated via POD, the real-space distributions of the predominant diabatic states were analyzed for the representative donor−framework interface (Figure S6). The spatial isosurfaces reveal that the diabatic states that contribute most significantly to the interfacial electronic coupling are strongly localized near the specific adsorption site, with direct orbital overlap between the functionalized pore wall and the adsorbed sacrificial molecule. In contrast, diabatic states delocalized across distant segments of the COF backbone display negligible spatial overlap with the adsorbate, yielding minor contributions to the overall coupling strength. This spatial localization confirms that the interfacial charge-transfer kinetics are predominantly governed by local electronic interactions at the binding site rather than nonspecific, long-range backbone states.

Finally, although the overall reaction involves water splitting, we do not explicitly consider charge transfer from the COF surface to water, as no clear correlation was observed between the corresponding computed rates and the experimental hydrogen evolution yields reported in ref 38. In contrast, a systematic correlation is obtained for hole transfer to the sacrificial agent (ascorbic acid) and electron transfer to the Pt cocatalyst, indicating that these pathways dominate the operative mechanism. In such systems, the oxidation half-reaction is typically governed by the sacrificial donor rather than water, and the identity of the effective proton source remains an open question. This raises the possibility that the proton source for hydrogen evolution may originate in the sacrificial agent itself, an interpretation consistent with prior reports in the literature.[69]

The overall trend in charge-transfer kinetics, −H < −Cl < −F, can be rationalized in terms of substituent-induced electronic effects, consistent with the interfacial and energetic considerations discussed above. The strong negative inductive ($-I$) effect of fluorine stabilizes charge-separated states, enhances interfacial polarization, and increases electronic coupling at both donor and acceptor interfaces. Chlorine, while still electron-withdrawing, exerts a weaker inductive effect and is further influenced by steric effects, which reduce effective orbital overlap and result in intermediate rates. In contrast, the unsubstituted framework lacks these electronic advantages, leading to less efficient charge extraction and lower photocatalytic activity.

Importantly, the consistency between the calculated Marcus−Hush rates and the experimentally observed trends in hydrogen evolution indicates that the POD−Marcus−Hush workflow captures the underlying physics governing photocatalytic activity. While the comparison is not intended to be quantitatively predictive in absolute terms, due to the inherent approximations in the model, it provides a reliable basis for assessing relative trends in catalytic performance. On this basis, we extend the analysis to a series of hypothetical functionalizations, employing the same rate-based descriptors to evaluate their expected photocatalytic behavior.

Extension to Hypothetical Functionalizations. Having established quantitative agreement between POD-derived Marcus−Hush rates and experimental hydrogen evolution for the halogen-substituted COFs, we next extend this validated framework to a series of hypothetical functionalizations (−Br, −CN, $-NO_2$, and −COOH) to assess their potential photocatalytic performance. The corresponding POD-resolved DOS and coupling distributions for the acid−COF and Pt−COF interfaces are reported in Figures S4 and S5, while the computed charge-transfer rates are included in Table 2 and Figure 7. The electron-transfer behavior of the −CN− functionalized COF provides a clear illustration of how individual strongly coupled states can dominate interfacial kinetics. As shown in Figure S4d, the CN-COF−Pt interface exhibits a distinct COF-derived state with an electronic coupling approaching 0.2 eV—significantly larger than the surrounding manifold. Crucially, this state is energetically aligned such that electron transfer from the COF conduction-band edge to the Pt LUMO is downhill. The presence of such highly coupled, energetically favorable channels leads to a substantial enhancement of the electron-transfer rate in CN-COF (7.65×10^{12} s^{-1}), markedly exceeding that of Br-COF (1.89×10^{10} s^{-1}). In the Br-COF−Pt interface (Figure S4b), although states at higher energies exhibit sizable couplings, the COF states closest to the conduction-band edge—those expected to contribute most significantly to interfacial electron transfer following photoexcitation—show substantially weaker coupling, thereby limiting the overall electron-transfer rate. A similar energetic rationale explains the relative hole-transfer rates in these systems. In Br-COF, the HOMO of ascorbic acid lies significantly lower than the COF valence-band maximum, rendering hole transfer more energetically downhill and therefore less favorable compared to CN-COF. As a result, Br-COF exhibits a lower hole-transfer rate (1.64×10^{12} s^{-1}) than CN-COF (2.14×10^{12} s^{-1}).

The comparison between $-NO_2$ and −COOH functionalizations further highlights the interplay between energetic alignment and coupling strength. In the acid−COF interfaces (Figure S5a and c), hole transfer to the ascorbic-acid HOMO is more energetically downhill for −COOH−COF than for $-NO_2$−COF, leading to a reduced hole-transfer rate in the former (1.95×10^{12} s^{-1}) relative to the latter (2.23×10^{12} s^{-1}). In contrast, the Pt−COF interfaces (Figure S5b and d) show that electron transfer from the COF conduction band to the Pt LUMO is less uphill for −COOH−COF than for $-NO_2$−COF, owing to a smaller CBM−LUMO energy offset. This more favorable alignment outweighs differences in coupling magnitude and results in a higher electron-transfer rate for −COOH (1.59×10^{13} s^{-1}) compared to $-NO_2$−COF (1.25×10^{13} s^{-1}).

From a broader substituent perspective, these trends underscore that photocatalytic efficiency is not governed solely by inductive effects. While strongly electron-withdrawing groups with dominant negative inductive ($-I$) character—such as −F—consistently promote high charge-transfer rates, substituents with pronounced negative mesomeric ($-M$) effects (−CN, $-NO_2$, −COOH) introduce additional complexity through resonance-driven orbital reorganization and dipole modulation. The −Br substituent, which combines

https://doi.org/10.1021/acs.jpcc.6c03692
J. Phys. Chem. C XXXX, XXX, XXX−XXX

a weak $-I$ effect with a competing positive mesomeric $(+M)$ contribution, exemplifies this balance by exhibiting comparatively suppressed electron-transfer rates despite moderate hole extraction.

Overall, the analysis of hypothetical functionalizations confirms that POD-resolved energetic alignment and state-specific electronic couplings provide a robust, transferable basis for predicting interfacial charge-transfer kinetics. By capturing how individual substituents reshape the density and strength of electronically active channels, this framework enables rational screening of COF photocatalysts beyond empirically explored chemical space—an aspect we summarize in the concluding section.

4. CONCLUSION

In this work, we have established a coherent microscopic framework that connects excited-state photophysics, interfacial electronic structure, and charge-transfer kinetics to the photocatalytic hydrogen evolution performance of halogen- and functionally substituted COFs. By explicitly linking these processes to catalytically relevant charge-transfer steps, the present study provides a mechanistic foundation for understanding hydrogen evolution in COF-based systems. By combining real-time excited-state dynamics, transition contribution analyses, projected density of states, and POD-based electronic coupling calculations, we provide a unified description of how subtle chemical substitutions modulate exciton delocalization, initial electronic coherence, and ultimately interfacial charge extraction.

Time-resolved charge population analyses reveal that halogen substitution systematically alters early time carrier redistribution and separation dynamics, with fluorine and chlorine stabilizing charge-separated states through distinct but complementary mechanisms. Fluorination promotes efficient redistribution of electrons toward the conduction-band edge while maintaining high transient carrier densities, whereas chlorination favors deeper hole localization, enhancing oxidative driving forces. These substituent-dependent carrier redistribution patterns are entirely consistent with the observed differences in excitonic delocalization inferred from TCMs and the framework-centric nature of the optical excitations revealed by orbital-resolved DOS analyses.

At the interface level, POD analysis shows that halogen substitution enhances both hole- and electron-transfer couplings at the acid−COF and Pt−COF junctions, respectively, with fluorination providing the most balanced optimization of both processes. When combined with reorganization energies within the Marcus−Hush formalism, these couplings yield charge-transfer rates that reproduce the experimentally observed trends in hydrogen evolution activity across H-, Cl-, and F-COFs in a semiquantitative manner. Importantly, this agreement emerges without invoking empirical fitting, underscoring the physical robustness and comparative predictive capability of the approach.

Extension of the same formalism to hypothetical functionalizations highlights how individual strongly coupled electronic channels, energetic alignment, and substituent-induced polarization collectively govern interfacial kinetics. The contrasting behaviors of $-CN$, $-NO_2$, $-COOH$, and $-Br$ substitutions illustrate that neither binding strength nor dipole magnitude alone is sufficient to predict photocatalytic efficiency; instead, productive charge transfer is dictated by the presence of energetically downhill, strongly coupled states that remain accessible during the early time photoexcited carrier dynamics. These insights further reinforce the importance of interfacial charge-transfer kinetics as a unifying descriptor of catalytic performance.

In summary, our findings explicitly answer the three central questions posed in the Introduction: (1) sacrificial electron donors serve as the efficient hole-scavenging source, maintaining the proton supply for continuous turnover; (2) hole transfer proceeds via a nonadiabatic, donor-to-framework pathway mediated by electronic coupling with the conjugated backbone; and (3) charge separation is primarily dictated by halogen-induced local polarization, where fluorination significantly enhances interfacial coupling strengths (J_E) without altering the primary optical absorption edge.

Overall, this study demonstrates that POD-based electronic-coupling analysis, when integrated with excited-state dynamics and Marcus−Hush kinetics, provides a transferable, physically transparent strategy for evaluating and predicting photocatalytic performance in COFs. Rather than relying on static or purely electronic descriptors, the present framework establishes a direct connection between molecular-level excited-state processes and macroscopic catalytic activity. Beyond rationalizing existing experimental trends, this framework offers a robust platform for screening and designing next-generation organic photocatalysts, with direct applicability to extended π-conjugated materials, hybrid interfaces, and related light-driven energy conversion systems. In this context, the identified rate-based descriptors can, in principle, be employed for the prescreening of candidate materials prior to experimental realization, thereby accelerating the discovery of efficient photocatalysts.

■ ASSOCIATED CONTENT

Data Availability Statement

The data that support the findings of this study are available from the corresponding authors upon reasonable request.

Supporting Information

The Supporting Information is available free of charge at https://pubs.acs.org/doi/10.1021/acs.jpcc.6c03692.

Dipole response, evolution of photoinduced charge density, POD-derived frontier energy alignment, and electronic couplings (PDF)

■ AUTHOR INFORMATION

Corresponding Author

Anirban Mondal − *Department of Chemistry, Indian Institute of Technology Gandhinagar, Gandhinagar, Gujarat 382355, India*; orcid.org/0000-0003-3029-8840; Email: amondal@iitgn.ac.in

Author

Sohini Khan − *Department of Chemistry, Indian Institute of Technology Gandhinagar, Gandhinagar, Gujarat 382355, India*

Complete contact information is available at: https://pubs.acs.org/10.1021/acs.jpcc.6c03692

Author Contributions

A.M. conceived the problem. S.K. conducted all the simulations. S.K. and A.M. analyzed the results and prepared the draft.

https://doi.org/10.1021/acs.jpcc.6c03692
J. Phys. Chem. C XXXX, XXX, XXX−XXX

Notes

The authors declare no competing financial interest.

■ ACKNOWLEDGMENTS

The authors gratefully acknowledge the Indian Institute of Technology Gandhinagar, India, for providing research facilities and financial support. We thank PARAM Ananta for computational resources. We acknowledge Khushboo Bhardwaj (Indian Institute of Technology Madras) for her insightful discussions on setting up the TDDFT simulations.

■ REFERENCES

(1) Sebestyén, V. Renewable and Sustainable Energy Reviews: Environmental impact networks of renewable energy power plants. *Renewable Sustainable Energy Rev.* **2021**, *151*, No. 111626.
(2) Bellabarba, R.; Johnston, P.; Moss, S.; Sievers, C.; Subramaniam, B.; Tway, C.; Wang, Z.; Zhu, H. Net zero transition: possible implications for catalysis. *ACS Catal.* **2023**, *13*, 7917−7928.
(3) Achakulwisut, P.; Erickson, P.; Guivarch, C.; Schaeffer, R.; Brutschin, E.; Pye, S. Global fossil fuel reduction pathways under different climate mitigation strategies and ambitions. *Nat. Commun.* **2023**, *14*, No. 5425.
(4) Chu, S.; Majumdar, A. Opportunities and challenges for a sustainable energy future. *Nature* **2012**, *488*, 294−303.
(5) Segura, C.; Flores, M. E.; Osorio-Román, I.; Jara-Quinteros, D. H.; Yoon, S. J.; Gualdrón-Reyes, A. F. Lead-Free Perovskite-Based Photocatalysts for Solar-Driven Chemistry Technologies. *ChemistrySelect* **2024**, *9*, No. e202305225.
(6) Maeda, K.; Domen, K. Photocatalytic water splitting: recent progress and future challenges. *J. Phys. Chem. Lett.* **2010**, *1*, 2655−2661.
(7) Møller, K. T.; Jensen, T. R.; Akiba, E.; Li, H.-w. Hydrogen-A sustainable energy carrier. *Prog. Nat. Sci.: Mater. Int.* **2017**, *27*, 34−40.
(8) Hisatomi, T.; Wang, Q.; Zhang, F.; Ardo, S.; Reisner, E.; Nishiyama, H.; Kudo, A.; Yamada, T.; Domen, K. Photocatalytic water splitting for large-scale solar-to-chemical energy conversion and storage. *Front. Sci.* **2024**, *2*, No. 1411644.
(9) Fu, H.; Wu, Y.; Guo, Y.; Sakurai, T.; Zhang, Q.; Liu, Y.; Zheng, Z.; Cheng, H.; Wang, Z.; Huang, B.; Wang, Q.; Domen, K.; Wang, P. A scalable solar-driven photocatalytic system for separated H2 and O2 production from water. *Nat. Commun.* **2025**, *16*, No. 990.
(10) Lin, L.; Ma, Y.; Vequizo, J. J. M.; Nakabayashi, M.; Gu, C.; Tao, X.; Yoshida, H.; Pihosh, Y.; Nishina, Y.; Yamakata, A.; Shibata, N.; Hisatomi, T.; Takata, T.; Domen, K. Efficient and stable visible-light-driven Z-scheme overall water splitting using an oxysulfide H2 evolution photocatalyst. *Nat. Commun.* **2024**, *15*, No. 397.
(11) Chen, S.; Takata, T.; Domen, K. Particulate photocatalysts for overall water splitting. *Nat. Rev. Mater.* **2017**, *2*, 1−17.
(12) Xing, J.; Fang, W. Q.; Zhao, H. J.; Yang, H. G. Inorganic photocatalysts for overall water splitting. *Chem. - Asian J.* **2012**, *7*, 642−657.
(13) Osterloh, F. E. Inorganic nanostructures for photoelectrochemical and photocatalytic water splitting. *Chem. Soc. Rev.* **2013**, *42*, 2294−2320.
(14) Khan, S.; Patrikar, K.; Sewak, R.; Mondal, A. Correlating Ligand Properties with Photocatalytic Efficiency: A Computational Framework for Interface Engineering. *ACS Appl. Mater. Interfaces* **2025**, *17*, 32306−32315, DOI: 10.1021/acsami.5c03069.
(15) Kazuma, E.; Kim, Y. Mechanistic studies of plasmon chemistry on metal catalysts. *Angew. Chem., Int. Ed.* **2019**, *58*, 4800−4808.
(16) Narzary, S.; Duraisamy, K.; Medikondu, N. R.; Chakraborty, K.; Das, S.; Choudhury, M. G.; Paul, S. Recent trends on perovskite materials and their applications in photocatalysis: a review. *Opt. Quantum. Electron.* **2024**, *56*, No. 1665.
(17) Zhang, G.; Liu, G.; Wang, L.; Irvine, J. T. Inorganic perovskite photocatalysts for solar energy utilization. *Chem. Soc. Rev.* **2016**, *45*, 5951−5984.
(18) Huang, H.; Pradhan, B.; Hofkens, J.; Roeffaers, M. B.; Steele, J. A. Solar-driven metal halide perovskite photocatalysis: design, stability, and performance. *ACS Energy Lett.* **2020**, *5*, 1107−1123.
(19) DuBose, J. T.; Kamat, P. V. Efficacy of perovskite photocatalysis: challenges to overcome. *ACS Energy Lett.* **2022**, *7*, 1994−2011.
(20) Li, R.; Wang, X.; Chen, M. Non-noble metal and nonmetallic plasmonic nanomaterials with located surface plasmon resonance effects: Photocatalytic performance and applications. *Catalysts* **2023**, *13*, No. 940.
(21) Waller, P. J.; Gándara, F.; Yaghi, O. M. Chemistry of covalent organic frameworks. *Acc. Chem. Res.* **2015**, *48*, 3053−3063.
(22) Khalil, I. E.; Das, P.; Thomas, A. Two-dimensional covalent organic frameworks: structural insights across different length scales and their impact on photocatalytic efficiency. *Acc. Chem. Res.* **2024**, *57*, 3138−3150.
(23) Wu, X.; Sayed, M.; Wang, G.; Yu, W.; Zhu, B. COF-based S-scheme heterojunction photocatalyst. *Adv. Mater.* **2026**, *38*, No. e11322.
(24) Keller, N.; Bein, T. Optoelectronic processes in covalent organic frameworks. *Chem. Soc. Rev.* **2021**, *50*, 1813−1845.
(25) López-Magano, A.; Daliran, S.; Oveisi, A. R.; Mas-Ballesté, R.; Dhakshinamoorthy, A.; Alemán, J.; Garcia, H.; Luque, R. Recent advances in the use of covalent organic frameworks as heterogenous photocatalysts in organic synthesis. *Adv. Mater.* **2023**, *35*, No. 2209475.
(26) Qi, S.-p.; Guo, R.-t.; Bi, Z.-x.; Zhang, Z.-r.; Li, C.-f.; Pan, W.-g. Recent progress of covalent organic frameworks-based materials in photocatalytic applications: a review. *Small* **2023**, *19*, No. 2303632.
(27) Blätte, D.; Ortmann, F.; Bein, T. Photons, excitons, and electrons in covalent organic frameworks. *J. Am. Chem. Soc.* **2024**, *146*, 32161−32205.
(28) Khalil, I. E.; Das, P.; Thomas, A. Two-Dimensional covalent organic frameworks: structural insights across different length scales and their impact on photocatalytic efficiency. *Acc. Chem. Res.* **2024**, *57*, 3138−3150.
(29) Liu, M.; Chen, Y.-J.; Huang, X.; Dong, L.-Z.; Lu, M.; Guo, C.; Yuan, D.; Chen, Y.; Xu, G.; Li, S.-L.; Lan, Y.-Q. Porphyrin-based COF 2D materials: variable modification of sensing performances by post-metallization. *Angew. Chem., Int. Ed.* **2022**, *61*, No. e202115308.
(30) Liu, W.; Li, X.; Wang, C.; Pan, H.; Liu, W.; Wang, K.; Zeng, Q.; Wang, R.; Jiang, J. A scalable general synthetic approach toward ultrathin imine-linked two-dimensional covalent organic framework nanosheets for photocatalytic CO2 reduction. *J. Am. Chem. Soc.* **2019**, *141*, 17431−17440.
(31) Stegbauer, L.; Schwinghammer, K.; Lotsch, B. V. A hydrazone-based covalent organic framework for photocatalytic hydrogen production. *Chem. Sci.* **2014**, *5*, 2789−2793.
(32) Banerjee, T.; Gottschling, K.; Savasci, G.; Ochsenfeld, C.; Lotsch, B. V. H2 evolution with covalent organic framework photocatalysts. *ACS Energy Lett.* **2018**, *3*, 400−409.
(33) Khalil, I. E.; Das, P.; Thomas, A. Two-dimensional covalent organic frameworks: Structural insights across different length scales and their impact on photocatalytic efficiency. *Acc. Chem. Res.* **2024**, *57*, 3138−3150.
(34) Mourino, B.; Jablonka, K. M.; Ortega-Guerrero, A.; Smit, B. In Search of Covalent Organic Framework Photocatalysts: A DFT-Based Screening Approach. *Adv. Funct. Mater.* **2023**, *33*, No. 2301594.
(35) Qin, L.; Ma, C.; Zhang, J.; Zhou, T. Structural motifs in covalent organic frameworks for photocatalysis. *Adv. Funct. Mater.* **2024**, *34*, No. 2401562.
(36) Zhang, J.; Li, X.; Hu, H.; Huang, H.; Li, H.; Sun, X.; Ma, T. Enhancing photocatalytic performance of covalent organic frameworks via ionic polarization. *Nat. Commun.* **2024**, *15*, No. 9576.
(37) Qian, Y.; Han, Y.; Zhang, X.; Yang, G.; Zhang, G.; Jiang, H.-L. Computation-based regulation of excitonic effects in donor-acceptor covalent organic frameworks for enhanced photocatalysis. *Nat. Commun.* **2023**, *14*, No. 3083.

(38) Wang, M.; Wang, Z.; Shan, M.; Wang, J.; Qiu, Z.; Song, J.; Li, Z. Fluorine-Substituted Donor−Acceptor Covalent Organic Frameworks for Efficient Photocatalyst Hydrogen Evolution. *Chem. Mater.* **2023**, *35*, 5368−5377.
(39) Frisch, M. J.; Trucks, G. W.; Schlegel, H. B.; Scuseria, G. E.; Robb, M. A.; Cheeseman, J. R.; Scalmani, G.; Barone, V.; Mennucci, B.; Petersson, G. A.; Nakatsuji, H.; Caricato, M.; Li, X.; Hratchian, H. P.; Izmaylov, A. F.; Bloino, J.; Zheng, G.; Sonnenberg, J. L.; Hada, M.; Ehara, M.; Toyota, K.; Fukuda, R.; Hasegawa, J.; Ishida, M.; Nakajima, T.; Honda, Y.; Kitao, O.; Nakai, H.; Vreven, T.; Montgomery, J. A., Jr.; Peralta, J. E.; Ogliaro, F.; Bearpark, M.; Heyd, J. J.; Brothers, E.; Kudin, K. N.; Staroverov, V. N.; Kobayashi, R.; Normand, J.; Raghavachari, K.; Rendell, A.; Burant, J. C.; Iyengar, S. S.; Tomasi, J.; Cossi, M.; Rega, N.; Millam, J. M.; Klene, M.; Knox, J. E.; Cross, J. B.; Bakken, V.; Adamo, C.; Jaramillo, J.; Gomperts, R.; Stratmann, R. E.; Yazyev, O.; Austin, A. J.; Cammi, R.; Pomelli, C.; Ochterski, J. W.; Martin, R. L.; Morokuma, K.; Zakrzewski, V. G.; Voth, G. A.; Salvador, P.; Dannenberg, J. J.; Dapprich, S.; Daniels, A. D.; Farkas, Ã.; Foresman, J. B.; Ortiz, J. V.; Cioslowski, J.; Fox, D. J. *Gaussian 09 Revision E.01*; Gaussian Inc.: Wallingford CT, 2009.
(40) Hutter, J.; Iannuzzi, M.; Schiffmann, F.; VandeVondele, J. cp2k: atomistic simulations of condensed matter systems. *WIREs Comput. Mol. Sci.* **2014**, *4*, 15−25.
(41) VandeVondele, J.; Krack, M.; Mohamed, F.; Parrinello, M.; Chassaing, T.; Hutter, J. Quickstep: Fast and accurate density functional calculations using a mixed Gaussian and plane waves approach. *Comput. Phys. Commun.* **2005**, *167*, 103−128.
(42) Gottwald, F.; Penschke, C.; Saalfrank, P. Water splitting at imine-linked covalent organic frameworks. *Phys. Chem. Chem. Phys.* **2024**, *26*, 21821−21831.
(43) Sajid, H. Effect of interlayer slipping on the geometric, thermal and adsorption properties of 2D covalent organic frameworks: a comprehensive review based on computational modelling studies. *Phys. Chem. Chem. Phys.* **2024**, *26*, 8577−8603.
(44) Perdew, J. P.; Burke, K.; Ernzerhof, M. Generalized gradient approximation made simple. *Phys. Rev. Lett.* **1996**, *77*, No. 3865.
(45) Grimme, S.; Antony, J.; Ehrlich, S.; Krieg, H. A consistent and accurate ab initio parametrization of density functional dispersion correction (DFT-D) for the 94 elements H-Pu. *J. Chem. Phys.* **2010**, *132*, No. 154104, DOI: 10.1063/1.3382344.
(46) Goedecker, S.; Teter, M.; Hutter, J. Separable dual-space Gaussian pseudopotentials. *Phys. Rev. B* **1996**, *54*, No. 1703.
(47) Hartwigsen, C.; Gœdecker, S.; Hutter, J. Relativistic separable dual-space Gaussian pseudopotentials from H to Rn. *Phys. Rev. B* **1998**, *58*, No. 3641.
(48) Mortensen, J. J.; Hansen, L. B.; Jacobsen, K. W. Real-space grid implementation of the projector augmented wave method. *Phys. Rev. B* **2005**, *71*, No. 035109.
(49) Enkovaara, J.; Rostgaard, C.; Mortensen, J. J.; Chen, J.; Dułak, M.; Ferrighi, L.; Gavnholt, J.; Glinsvad, C.; Haikola, V.; Hansen, H. A.; Kristoffersen, H. H.; Kuisma, M.; Larsen, A. H.; Lehtovaara, L.; Ljungberg, M.; Lopez-Acevedo, O.; Moses, P. G.; Ojanen, J.; Olsen, T.; Petzold, V.; Romero, N. A.; Stausholm-Møller, J.; Strange, M.; Tritsaris, G. A.; Vanin, M.; Walter, M.; Hammer, B.; Häkkinen, H.; Madsen, G. K. H.; Nieminen, R. M.; Nørskov, J. K.; Puska, M.; Rantala, T. T.; Schiøtz, J.; Thygesen, K. S.; Jacobsen, K. W. Electronic structure calculations with GPAW: a real-space implementation of the projectoraugmented-wave method. *J. Phys.: Condens. Matter* **2010**, *22*, No. 253202.
(50) Larsen, A. H.; Mortensen, J. J.; Blomqvist, J.; Castelli, I. E.; Christensen, R.; Dułak, M.; Friis, J.; Groves, M. N.; Hammer, B.; Hargus, C. H.; Hermes, E. D.; Jennings, P. C.; Jensen, P. B.; Kermode, J.; Kitchin, J. R.; Kolsbjerg, E. L.; Kubal, J.; Kaasbjerg, K.; Lysgaard, S.; Maronsson, J. B.; Maxson, T.; Olsen, T.; Pastewka, L.; Peterson, A.; Rostgaard, C.; Schiøtz, J.; Schütt, O.; Strange, M.; Thygesen, K. S.; Vegge, T.; Vilhelmsen, L.; Walter, M.; Zeng, Z.; Jacobsen, K. W. The atomic simulation environment−a Python library for working with atoms. *J. Phys.: Condens. Matter* **2017**, *29*, No. 273002.
(51) Larsen, A. H.; Vanin, M.; Mortensen, J. J.; Thygesen, K. S.; Jacobsen, K. W. Localized atomic basis set in the projector augmented wave method. *Phys. Rev. B* **2009**, *80*, No. 195112.
(52) Verma, P. K.; Nayak, S. K.; Bhardwaj, K.; Yamijala, S. S. Realizing Direct Hot-Electron Transfer from Metal Nanoparticles to Per-and Polyfluoroalkyl Substances. *J. Phys. Chem. Lett.* **2025**, *16*, 4536−4546.
(53) Fojt, J.; Rossi, T. P.; Kuisma, M.; Erhart, P. Hot-carrier transfer across a nanoparticle-molecule junction: The importance of orbital hybridization and level alignment. *Nano Lett.* **2022**, *22*, 8786−8792.
(54) Rossi, T. P.; Erhart, P.; Kuisma, M. Hot-carrier generation in plasmonic nanoparticles: the importance of atomic structure. *ACS Nano* **2020**, *14*, 9963−9971.
(55) Joshi, G.; Patrikar, K.; Singhal, U.; Mondal, A.; Khatua, S. Controlling plasmonic charge carrier flow at a nanoparticle−molecule interface using ligand chemistry. *Nanoscale* **2025**, *17*, 23315−23322.
(56) Futera, Z.; Blumberger, J. Electronic couplings for charge transfer across molecule/metal and molecule/semiconductor interfaces: Performance of the projector operator-based diabatization approach. *J. Phys. Chem. C* **2017**, *121*, 19677−19689.
(57) Ziogos, O. G.; Kubas, A.; Futera, Z.; Xie, W.; Elstner, M.; Blumberger, J. HAB79: A new molecular dataset for benchmarking DFT and DFTB electronic couplings against high-level ab initio calculations. *J. Chem. Phys.* **2021**, *155*, No. 234115.
(58) Ghan, S.; Kunkel, C.; Reuter, K.; Oberhofer, H. Improved Projection-Operator Diabatization Schemes for the Calculation of Electronic Coupling Values. *J. Chem. Theory Comput.* **2020**, *16*, 7431−7443.
(59) Li, W.; Giannini, S.; Quarti, C.; Hou, Z.; Prezhdo, O. V.; Beljonne, D. Interlayer Charge Transport in 2D Lead Halide Perovskites from First Principles. *J. Chem. Theory Comput.* **2023**, *19*, 9403−9415.
(60) Stippell, E.; Li, W.; Quarti, C.; Beljonne, D.; Prezhdo, O. V. Enhancing interlayer charge transport of two-dimensional perovskites by structural stabilization via fluorine substitution. *ACS Appl. Mater. Interfaces* **2025**, *17*, 2032−2040.
(61) Xie, W.-L.; Zhang, Z.-H.; Yang, C.-L.; Wang, M.-S.; Ma, X.-G. Pt4 cluster catalyzes H2 generation from an H2O molecule. *Chem. Phys. Lett.* **2019**, *725*, 97−101.
(62) Roudgar, A.; Eikerling, M.; van Santen, R. Ab initio study of oxygen reduction mechanism at Pt4 cluster. *Phys. Chem. Chem. Phys.* **2010**, *12*, 614−620.
(63) Jia, Y.; Zhang, J.; Liu, Y.; Jing, J.; Li, W.-Y. Synergistic Cu +/Cu0 optimization via reduction-induced activation for water-gas shift reaction over Cu/Fe3O4 catalyst. *J. Energy Inst.* **2025**, *123*, No. 102288.
(64) Tan, R.; Zhuge, K.; Ma, X.; Mou, X.; Ren, M.; Chang, R.; Zhou, Q.; Yan, L.; Lin, R.; Ding, Y. Interfacial effects of Cu/Fe3O4 in water-gas shift reaction: Role of Fe3O4 crystallite sizes. *Int. J. Hydrogen Energy* **2024**, *78*, 741−752.
(65) Berlin, Y. A.; Hutchison, G. R.; Rempala, P.; Ratner, M. A.; Michl, J. Charge hopping in molecular wires as a sequence of electron-transfer reactions. *J. Phys. Chem. A* **2003**, *107*, 3970−3980.
(66) Marcus, R. A. On the Theory of Electron-transfer Reactions. VI. Unified Treatment for Homogeneous and Electrode Reactions. *J. Chem. Phys.* **1965**, *43*, 679−701.
(67) Hush, N. S. Adiabatic Rate Processes at Electrodes. I. Energy-charge Relationships. *J. Chem. Phys.* **1958**, *28*, 962−972.
(68) Patrikar, K.; Rao, V. R.; Kabra, D.; Mondal, A. Understanding the microscopic origin of the contact resistance at the polymer-electrode interface. *ACS Appl. Mater. Interfaces* **2023**, *15*, 49427−49435.
(69) Weng, W.; Guo, J. The effect of enantioselective chiral covalent organic frameworks and cysteine sacrificial donors on photocatalytic hydrogen evolution. *Nat. Commun.* **2022**, *13*, No. 5768.